ARTICLE

doi:10.1038/nature12742

Context-dependent computation by recurrent dynamics in prefrontal cortex

Valerio Mante[1]†*, David Sussillo[2]*, Krishna V. Shenoy[2,3] & William T. Newsome[1]

Prefrontal cortex is thought to have a fundamental role in flexible, context-dependent behaviour, but the exact nature of the computations underlying this role remains largely unknown. In particular, individual prefrontal neurons often generate remarkably complex responses that defy deep understanding of their contribution to behaviour. Here we study prefrontal cortex activity in macaque monkeys trained to flexibly select and integrate noisy sensory inputs towards a choice. We find that the observed complexity and functional roles of single neurons are readily understood in the framework of a dynamical process unfolding at the level of the population. The population dynamics can be reproduced by a trained recurrent neural network, which suggests a previously unknown mechanism for selection and integration of task-relevant inputs. This mechanism indicates that selection and integration are two aspects of a single dynamical process unfolding within the same prefrontal circuits, and potentially provides a novel, general framework for understanding context-dependent computations.

Our interactions with the world are inherently flexible. Identical sensory stimuli, for example, can lead to very different behavioural responses depending on 'context', which includes goals, previous expectations about upcoming events, and relevant past experiences[1,2]. Animals can switch rapidly between behavioural contexts, implying the existence of rapid modulation, or 'gating', mechanisms within the brain that select relevant sensory information for decision-making and action. A large attention literature suggests that relevant information is selected by top-down modulation of neural activity in early sensory areas[3–8], which may take the form of modulation of firing rates[3,5–7], or modulation of response synchrony within or across areas[4,5,8]. The top-down signals underlying such 'early' modulations of sensory activity arise, in part, from prefrontal cortex (PFC)[2,5], which is known to contribute to representing and maintaining contextual knowledge, ignoring irrelevant information, and suppressing inappropriate actions[1,2,9,10]. These observations have led to the hypothesis that early selection may account for the larger effect of relevant as compared to irrelevant sensory information on contextually sensitive behaviour.

Here we test this hypothesis with a task requiring context-dependent selection and integration of visual stimuli. We trained two macaque monkeys (A and F) to perform two different perceptual discriminations on the same set of visual stimuli (Fig. 1). The monkeys were instructed by a contextual cue to either discriminate the direction of motion or the colour of a random-dot display, and to report their choices with a saccade to one of two visual targets (Fig. 1a). While monkeys performed this task, we recorded extracellular responses from neurons in and around the frontal eye field (Extended Data Fig. 1a, f), an area of PFC involved in the selection and execution of saccadic eye movements[11,12], the control of visuo-spatial attention[13], and the integration of information towards visuomotor decisions[12,14].

We found no evidence that irrelevant sensory inputs are gated, or filtered out, before the integration stage in PFC, as would be expected from early selection mechanisms[3–8]. Instead, the relevant input seems to be selected late, by the same PFC circuitry that integrates sensory evidence towards a choice. Selection within PFC without previous gating is possible because the representations of the inputs, and of the upcoming choice, are separable at the population level, even though they are deeply entwined at the single neuron level. An appropriately trained recurrent neural network model reproduces key physiological observations and suggests a new mechanism of input selection and integration. The mechanism reflects just two learned features of a dynamical system: an approximate line attractor and a 'selection vector', which are only defined at the level of the population. The model mechanism is readily scalable to large numbers of inputs, indicating a general solution to the problem of context-dependent computation.

Behaviour and single-unit responses

The monkeys successfully discriminated the relevant sensory evidence in each context, while largely ignoring the irrelevant evidence (Fig. 1c–f, monkey A; Extended Data Fig. 2a–d, monkey F). To vary the difficulty of the discrimination, we changed the strength of the motion and colour signals randomly from trial to trial (Fig. 1b). In the motion context, the choices of the monkeys depended strongly on the direction of motion of the dots (Fig. 1c), whereas the choices depended only weakly on colour in the same trials (Fig. 1d). The opposite pattern was evident in the colour context: the now relevant colour evidence exerted a large effect on choices (Fig. 1f) whereas motion had only a weak effect (Fig. 1e).

As is common in PFC[1,2,15–18], the recorded responses of single neurons appeared to represent several different task-related signals at once, including the monkey's upcoming choice, the context, and the strength of motion and colour evidence (Extended Data Figs 1 and 3). Rather than attempting to understand the neural mechanism underlying selective integration by studying the responses of single PFC neurons, we focussed on analysing the responses of the population as a whole. To construct population responses, we pooled data from both single and multi-unit recordings, which yielded equivalent results. The great majority of units were not recorded simultaneously, but rather in separate sessions. Units at all recording locations seemed to contribute to the task-related signals analysed below (Extended Data Fig. 1) and were thus combined.

[1]Howard Hughes Medical Institute and Department of Neurobiology, Stanford University, Stanford, California 94305, USA. [2]Department of Electrical Engineering and Neurosciences Program, Stanford University, Stanford, California 94305, USA. [3]Departments of Neurobiology and Bioengineering, Stanford University, Stanford, California 94305, USA. †Present address: Institute of Neuroinformatics, University of Zurich/ETH Zurich, CH-8057 Zurich, Switzerland.
*These authors contributed equally to this work.

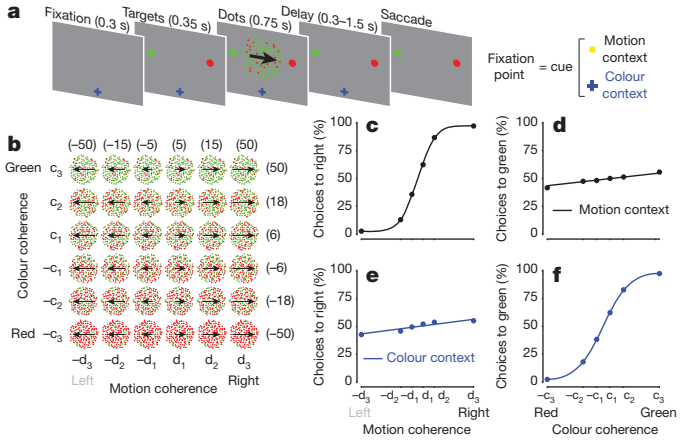

Figure 1 | Behavioural task and psychophysical performance. **a**, Task structure. Monkeys were instructed by a contextual cue to either discriminate the motion or the colour of a random-dot stimulus, and indicate their choice with a saccade to one of two targets. Depending on context, monkeys were rewarded for choosing the target matching the prevalent direction of motion (motion context) or the prevalent colour (colour context) of the random dots. Context was indicated by the shape and colour of the fixation point; offset of the fixation point was the 'go cue', signalling the monkey to indicate its choice via the operant saccade. **b**, Stimulus set. The motion and colour coherence of the dots was chosen randomly on each trial. We slightly varied the coherence values on each day, to equate performance across contexts and sessions (numbers in parentheses: average coherences (%) across sessions for monkey A). **c**–**f**, Psychophysical performance for monkey A in the motion (top) and colour contexts (bottom), averaged over 80 recording sessions (163,187 trials). Performance is shown as a function of motion (left) or colour (right) coherence in each behavioural context. The curves are fits of a behavioural model.

Overall, we analysed 388 single-unit and 1,014 multi-unit responses from the two monkeys.

State space analysis

To study how the PFC population as a whole dynamically encodes the task variables underlying the monkeys' behaviour, we represent population responses as trajectories in neural state space[17,19–25]. Each point in state space corresponds to a unique pattern of neural activations across the population. Because activations are dynamic, changing over time, the resulting population responses form trajectories in state space.

We focussed our analyses on responses in a specific low-dimensional subspace that captures across-trial variance due to the choice of the monkey (choice 1 or 2), the strength and direction of the motion evidence, the strength and direction of the colour evidence, and context (motion or colour). We estimated this task-related subspace in two steps (Supplementary Information). First, we used principal component analysis (PCA) to obtain an unbiased estimate of the most prominent features (that is, patterns of activations) in the population response. To 'de-noise' the population responses, we restricted subsequent analyses to the subspace spanned by the first 12 principal components. Second, we used linear regression to define the four orthogonal, task-related axes of choice, motion, colour and context. The projection of the population response onto these axes yields de-mixed estimates of the corresponding task variables, which are mixed both at the level of single neurons (Extended Data Fig. 3) and at the level of individual principal components (Extended Data Fig. 4c, g; see also ref. 26).

This population analysis yields highly reliable average response trajectories (Fig. 2 and Extended Data Fig. 4q, r) that capture both the temporal dynamics and the relationships among the task variables represented in PFC. In particular, four properties of the population responses provide fundamental constraints on the mechanisms of selection and integration underlying behaviour in our task.

First, integration of evidence during presentation of the random dots corresponds to a gradual movement of the population response in state space along the axis of choice (Fig. 2a, f). In both contexts, the trajectories start from a point in state space close to the centre of the plots ('dots on', purple point), which corresponds to the pattern of population responses at baseline. During the dots presentation the responses then quickly move away from this baseline level, along the axis of choice (red line; Fig. 2a, f). Overall, the population response moves in opposite directions on trials corresponding to the two different saccade directions (Fig. 2, choice 1 versus choice 2). The projection of the population response onto the choice axis (Extended Data Fig. 5b, f) is largely analogous to the 'choice-predictive' signals that have been identified in past studies as approximate integration of evidence during direction discrimination tasks[27].

Second, the sensory inputs into PFC produce patterns of population responses that are very different from those corresponding to either choice, meaning that these signals are separable at the level of the population. Indeed, the population response does not follow straight paths along the choice axis, but instead forms prominent arcs away from it (Fig. 2a, f). The magnitude of each arc along the axes of motion or colour reflects the strength of the corresponding sensory evidence (see scale), whereas its direction (up or down) reflects the sign of the evidence (towards choice 1 or 2, filled or empty symbols, respectively). Whereas the integrated evidence continues to be represented along the axis of choice even after the disappearance of the random dots ('dots off'), the signals along the axes of motion and colour are transient—the arcs return to points near the choice axis by the time of dots offset. These signals thus differ from integrated evidence both in terms of the corresponding patterns of activation and in their temporal profile. For these reasons, we interpret them as 'momentary evidence' from the motion and colour inputs in favour of the two choices. This interpretation is also consistent with the observed population responses on error trials, for which the momentary evidence points towards the chosen target, but is weaker than on correct trials (Extended Data Fig. 5c, d; red curves).

Third, context seems to have no substantial effect on the direction of the axes of choice, motion and colour, and only weak effects on the strength of the signals represented along these axes. When estimated separately during the motion and colour contexts, the two resulting sets of axes span largely overlapping subspaces (see Supplementary Table 1); thus, a single set of three axes (the red, black and blue axes in Fig. 2a–f, estimated by combining trials across contexts) is sufficient to capture the effects of choice, motion and colour on the population responses in either context. A comparison of the population responses across contexts (Fig. 2a–c versus d–f) reveals that a single, stable activity pattern is responsible for integrating the relevant evidence in both contexts (the choice axis), while similarly stable activity patterns represent the momentary motion and colour evidence in both contexts (motion and colour axes). Notably, motion and colour inputs result in comparable deflections along the motion and colour axes, respectively, whether they are relevant or not (compare Fig. 2a to d and f to c).

Fourth, although the directions of the axes of choice, motion and colour are largely invariant with context, their location in state space is not. The responses during the motion and colour contexts occupy different parts of state space, and the corresponding trajectories are well separated along the axis of context (Extended Data Fig. 6a, b).

Comparison to models of selection and integration

These properties of the population responses, which are summarized schematically in Fig. 3a, can be compared to the predictions of current models of context-dependent selection and integration (Fig. 3b–d). We first focussed on three fundamentally different mechanisms of selection that could each explain why the motion input, for example, influences choices in the motion context (Fig. 3, top row) but not in the colour context (Fig. 3, bottom row). In the framework of our task the three models predict population responses that differ substantially

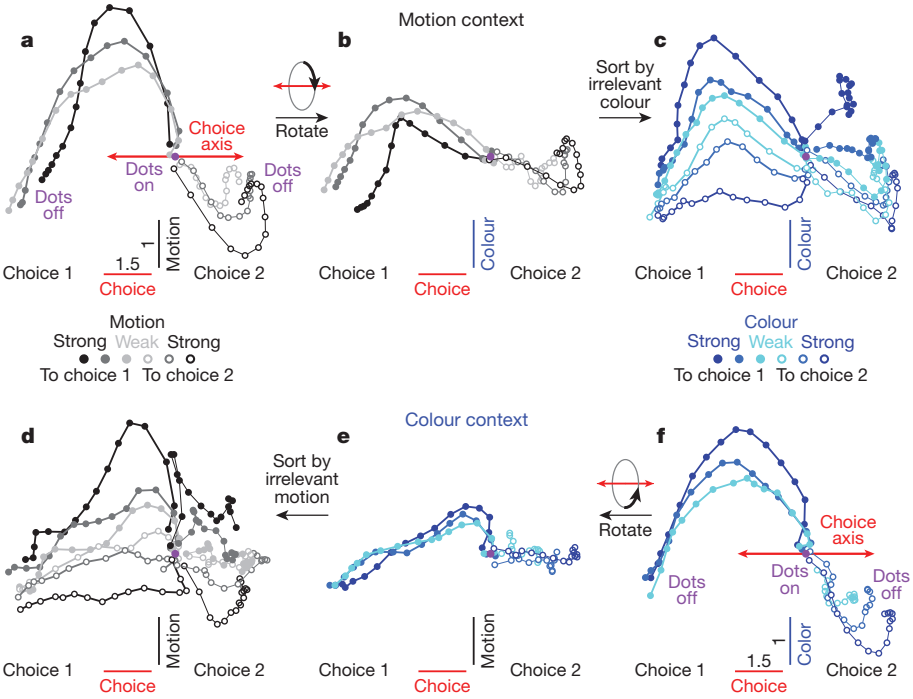

Figure 2 | Dynamics of population responses in PFC. The average population response for a given condition and time is represented as a point in state space. Responses from correct trials only are shown from 100 ms after dots onset (dots on, purple circle) to 100 ms after dots offset (dots off) in 50-ms steps, and are projected into the three-dimensional subspace capturing the variance due to the monkey's choice (along the choice axis), and to the direction and strength of the motion (motion axis) and colour (colour axis) inputs. Units are arbitrary; components along the motion and colour axes are enhanced relative to the choice axis (see scale bars in **a**, **f**). Conditions (see colour bars) are defined based on context (motion context, top; colour context, bottom), on the location of the chosen target (choice 1 versus choice 2) and either on the direction and strength of the motion (grey colours) or the colour input (blue colours). Here, choice 1 corresponds to the target in the response field of the recorded neurons. The direction of the colour input does not refer to the colour of the dots per se (red or green), but to whether the colour points towards choice 1 or choice 2 (see Supplementary Information, section 6.4, for a detailed description of the conditions). **a**, Effect of choice and the relevant motion input in the motion context, projected onto the axes of choice and motion. **b**, Same data as in **a**, but rotated by 90° around the axis of choice to reveal the projection onto the axis of colour. **c**, Same trials as in **b**, but re-sorted according to the direction and strength of the irrelevant colour input. **d**–**f**, Responses in the colour context, analogous to **a**–**c**. Responses are averaged to show the effects of the relevant colour (**e**, **f**) or the irrelevant motion input (**d**). For relevant inputs (**a**, **b** and **e**, **f**), correct choices occur only when the sensory stimulus points towards the chosen target (3 conditions per chosen target); for irrelevant inputs (**c**, **d**), however, the stimulus can point either towards or away from the chosen target on correct trials (6 conditions per chosen target).

from each other (Fig. 3b–d), and can thus be validated or rejected by our PFC recordings (Fig. 3a).

The first model (Fig. 3b) is based on two widely accepted hypotheses about the mechanisms underlying selection and integration of evidence. First, it assumes that inputs are selected early[3–8], such that a given input drives PFC responses when relevant (grey arrow in Fig. 3b, top), but is filtered out before reaching PFC when irrelevant (no grey arrow in Fig. 3b, bottom). Second, it assumes that the relevant input directly elicits a pattern of activation in PFC resembling the pattern corresponding to a choice (the grey arrow in Fig. 3b, top, points along the axis of choice), as would be expected by current models of integration[28,29].

Both hypotheses are difficult to reconcile with the recorded PFC responses. Whereas the strength of each input is reduced when it is irrelevant compared to when it is relevant, the magnitude of the observed reduction seems too small to account for the behavioural effects. For instance, irrelevant motion of high coherence (Fig. 2d, black) elicits a larger deflection along the motion axis (relative to baseline, purple dot, Fig. 2d) than relevant motion of intermediate coherence (Fig. 2a, dark grey). Yet the former has almost no behavioural effect (Fig. 1e), whereas the latter has a large behavioural effect (Fig. 1c). The analogous observation holds for the colour input (Figs 2c, f and 1d, f), strongly suggesting that the magnitude of the momentary evidence alone does not determine whether the corresponding input is integrated. Furthermore, the actual momentary motion input is represented along a direction that has little overlap with the choice axis, resulting in curved trajectories (Fig. 3a) that differ markedly from the straight trajectories predicted by the early selection model (Fig. 3b).

The observed PFC responses also rule out two additional models of selection presented in Fig. 3. In the absence of early selection, a motion input might be selected within PFC by modifying the angle between the choice and motion axes (that is, the similarity between patterns of neural activity representing choice and momentary motion evidence) across contexts. This angle could be modified either by changing the direction of the motion axis between contexts while keeping the choice axis fixed (Fig. 3c), or vice versa (Fig. 3d). In both cases, the motion input would elicit movement of the population along the axis of choice in the motion context (top row), but not in the colour context (bottom row), as the motion and choice axes have little or no overlap in the colour context. At the single neuron level, variable axes that change direction across contexts would be reflected as complex, nonlinear interactions between context and the other task variables, which have been proposed in some task-switching models[30,31]. However, our data (Figs 2 and 3a) lend little support for variable choice (Fig. 3d) or input (Fig. 3c) axes. More generally, the PFC data from monkey A rule out any model of integration for which the degree of overlap between the direction of the momentary evidence and the axis of choice determines how much the corresponding input affects behaviour.

The representation of task variables in PFC of monkey F replicates all but one key feature observed in monkey A. Most importantly, population responses along the choice and motion axes (Extended

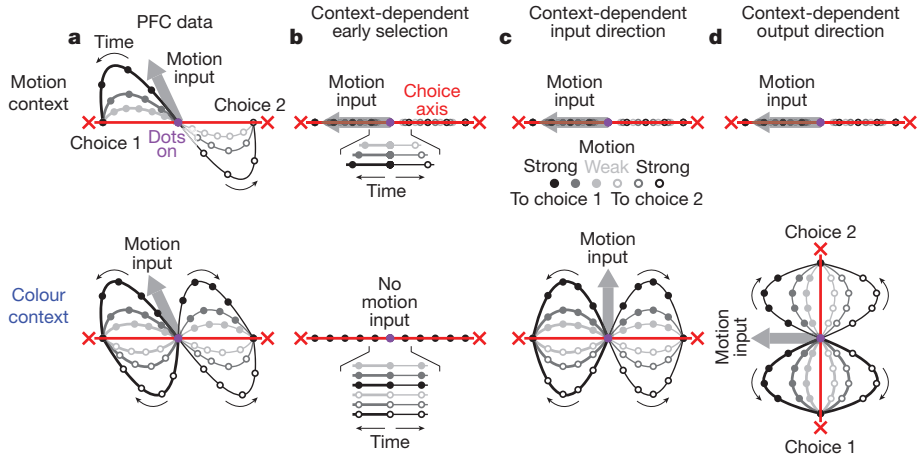

Figure 3 | Models of selective integration inconsistent with PFC responses. Schematic representation of population responses observed in PFC (**a**) and expected by several models of selective integration (**b**–**d**). The models differ from the PFC responses with respect to the relative directions and context dependence of the choice axis (red lines) and the inputs (thick grey arrows; only motion input is shown). The relevant input is integrated as movement along the choice axis towards one of two choices (red crosses). A motion input towards choice 1 'pushes' the responses along the direction of the grey arrow (towards choice 2: opposite direction). Same conditions as in Fig. 2a (motion context, top) and Fig. 2d (colour context, bottom). As in Fig. 2a and d, a single two-dimensional subspace (which contains the choice axis and motion input) is used to represent responses from both contexts. **a**, Idealized schematic of the actual PFC trajectories shown in Fig. 2a, d. Both the choice axis and motion input are stable between contexts. The motion input pushes the population response away from the choice axis. **b**, Early selection model. When relevant (top), the motion input pushes the population response along the choice axis. When irrelevant (bottom), the motion input is filtered out before reaching PFC (no thick grey arrow) and thus exerts no effect on choice. All trajectories fall on top of each other in both contexts, but the rate of movement along the choice axis increases with motion strength only in the motion context (insets show enlarged trajectories distributed vertically for clarity). **c**, Context-dependent input direction. Motion input direction varies between contexts, whereas the choice axis is stable. Inputs are not filtered out before PFC; rather, they are selected on the basis of their projection onto the choice axis. **d**, Context-dependent output direction. Similar selection mechanism to **c**, except that the choice axis varies between contexts, whereas the motion input is stable. The effects of the motion input on PFC responses in both monkeys (schematized in **a**) and the effects of the colour input in monkey A are inconsistent with predictions of the three models in **b**–**d** (respectively, Fig. 2a, d; Extended Data Fig. 7a,d; Fig. 2f, c).

Data Fig. 7a, d) closely match those observed in monkey A (Fig. 2a, d); thus, physiological data from both monkeys are consistent in rejecting current models of selection and integration of motion inputs (Fig. 3b–d). The colour signal in monkey F, however, is equivocal. On the one hand, the representation of the colour input closely resembles that of a choice (Extended Data Fig. 1g, i), as expected from the early selection model described above (Fig. 3b). On the other hand, the colour input is also weakly represented along the colour axis in both contexts (vertical displacement of trajectories, Extended Data Fig. 7c, f). For the colour input in monkey F, therefore, we cannot with confidence accept or reject the early selection model. Finally, as in monkey A, context is represented in monkey F along a separate axis of context (Extended Data Fig. 6c, d).

In summary, the population responses in both monkeys are difficult to reconcile with current models of selection and integration (see also Extended Data Fig. 8). Rather, the selective integration of the motion input in monkeys A and F, and of the colour input in monkey A, must rely on a mechanism for which the very same input into PFC leads to movement along a fixed axis of choice in one context but not another.

Recurrent network model of selection and integration

To identify such a mechanism, we trained a network of recurrently connected, nonlinear neurons[32] to solve a task analogous to the one solved by the monkeys (Fig. 4). Notably, we only defined 'what' the network should do, with minimal constraints on 'how' it should do it[32–34]. Thus, the solution achieved by the network is not hand-built into the network architecture. On each trial, neurons in the network receive two independent sensory inputs that mimic the momentary evidence for motion and colour in a single random dot stimulus. The network also receives a contextual input that mimics the contextual signal provided to the monkeys, instructing the network to discriminate either the motion or the colour input. The network activity is read out by a single linear read-out, corresponding to a weighted sum over the responses of all neurons in the network (see Supplementary Information). As in PFC, the contextual input does not affect the strength of the sensory inputs—selection occurs within the same network that integrates evidence towards a decision.

We trained the network[35] to make a binary choice on each trial—an output of +1 at the end of the stimulus presentation if the relevant evidence pointed leftward, or a −1 if it pointed rightward. After training, the model qualitatively reproduces the monkeys' behaviour,

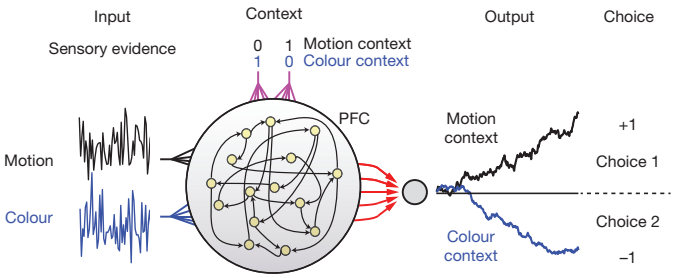

Figure 4 | A neural network model of input selection and integration. PFC is modelled as a network of recurrently connected, nonlinear, rate neurons that receive independent motion, colour and contextual inputs. The network is fully recurrently connected, and each unit receives both motion and colour inputs as well as two inputs that indicate context. At each time step, the sensory inputs are drawn from two normal distributions, the means of which correspond to the average strengths of the motion and colour evidence on a given trial. The contextual inputs take one of two values (0 or 1), which instruct the network to discriminate either the motion or the colour input. The network is read out by a single linear read-out, corresponding to a weighted sum over the responses of all neurons (red arrows). We trained the network (with back-propagation[35]) to make a binary choice, that is, to generate an output of +1 at the end of the stimulus presentation if the relevant evidence pointed towards choice 1, or a −1 if it pointed towards choice 2. Before training, all synaptic strengths were randomly initialized.

confirming that the model solves the selection problem at the 'behavioural' level (Extended Data Fig. 2e–h).

We first analysed model population trajectories in the subspace spanned by the axes of choice, motion and colour, and found that they reproduce the four main features of the PFC population responses discussed above (Fig. 5 and Extended Data Fig. 9a–g). First, integration of evidence corresponds to gradual movement of the population response along the choice axis. Second, momentary motion and colour evidence 'push' the population away from the choice axis, resulting in trajectories that are parametrically ordered along the motion and colour axes. Third, the direction of the axes of choice, motion and colour are largely invariant with context, as are the strength of the motion and colour inputs, as these are not gated before entering the network. Fourth, the trajectories during motion and colour contexts are separated along the axis of context (Extended Data Fig. 9f, g). Model and physiological dynamics differ markedly in one respect—signals along the input axes are transient in the physiology, but not in the model, yielding PFC trajectories that curve back to the choice axis before the end of the viewing interval (compare Figs 5a, f to 2a, f). This difference suggests that the sensory inputs to PFC are attenuated after a decision is reached. Additional differences between the model and the physiological dynamics can be readily explained by previously proposed imperfections in the evidence integration process, such as 'urgency' signals[36,37] or instability in the integrator[38] (Extended Data Fig. 10).

A novel mechanism of selective integration

We then 'reverse engineered' the model[33] to discover its mechanism of selective integration. The global features of the model activity are easily explained by the overall arrangement of fixed points of the dynamics[33] (Fig. 5), which result from the synaptic connectivity learned during training. Fixed points (small red crosses) correspond to patterns of neuronal activations (that is, locations in state space) that are stable when the sensory inputs are turned off. First, we found that the model generates a multitude of fixed points, which are approximately arranged to form two lines along the choice axis. The two sets of fixed points are separated along the axis of context (Extended Data Fig. 9f, g) and never exist together—one exists in the motion context (Fig. 5a–c), the other in the colour context (Fig. 5d–f). Second, the responses around each fixed point were approximately stable only along a single dimension pointing towards the neighbouring fixed points (red lines), whereas responses along any other dimension rapidly collapsed back to the fixed points. Therefore, each set of fixed points approximates a line attractor[39]. Finally, two stable attractors (large red crosses), corresponding to the two possible choices, delimit each line attractor.

The integration of the relevant evidence is thus implemented in the model as movement along an approximate line attractor[39]. The model population response, however, does not move strictly along the line attractor. Like the physiological data, model trajectories move parallel to the line attractors (the choice axis) at a distance proportional to the average strength of the sensory inputs, reflecting the momentary sensory evidence (Fig. 5a, c, d, f). After the inputs are turned off (Fig. 5, purple data points), the responses rapidly relax back to the line attractor.

To understand how the relevant input is selected for integration along a line attractor, we analysed the local dynamics of model responses around the identified fixed points[33] (Fig. 6). To simplify the analysis, we studied how the model responds to brief pulses of motion or colour inputs (Fig. 6a), rather than the noisy, temporally extended inputs used above. Before a pulse, we initialized the state of the network to one of the identified fixed points (Fig. 6a, red crosses). Locally around a fixed point, the responses of the full, nonlinear model can then be approximated by a linear dynamical system (see Supplementary Information), the dynamics of which can be more easily understood[33].

Both the motion and colour inputs (that is, the corresponding pulses) have substantial projections onto the line attractor (Fig. 6a) but, crucially, the size of these projections does not predict the extent to which each input will be integrated. For instance, in both contexts the motion pulses have similar projections onto the line attractor (Fig. 6a, left panels), and yet they result in large movement along the attractor in the motion context (top) but not in the colour context (bottom).

The selection of the inputs instead relies on context-dependent relaxation of the network dynamics after the end of the pulse, which reverses movement along the line attractor caused by the irrelevant pulse (Fig. 6a, top right and bottom left) and enhances the effects of the relevant pulse (Fig. 6a, top left and bottom right). These relaxation

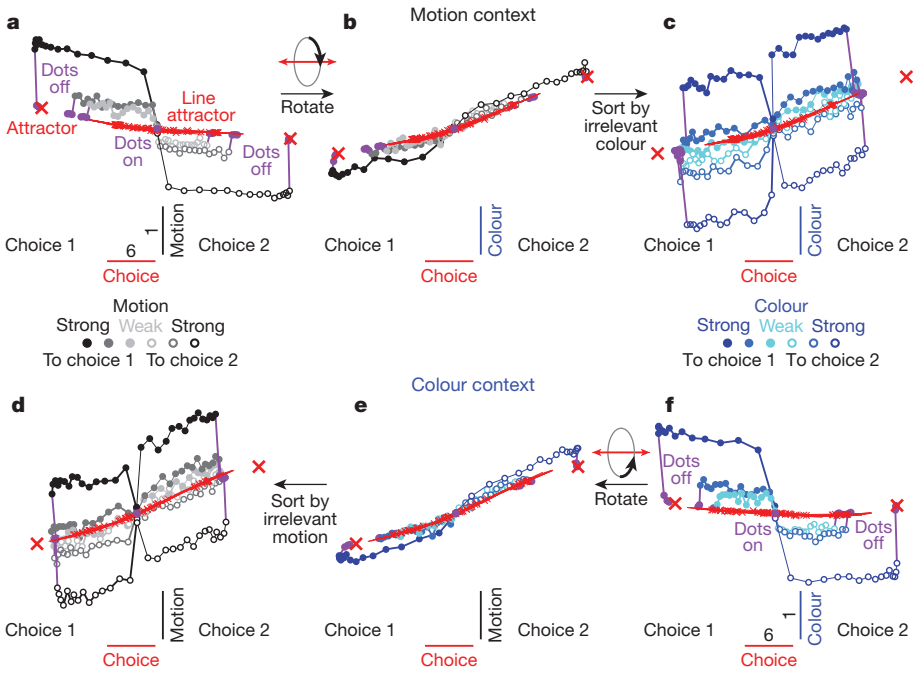

Figure 5 | Model dynamics and fixed points analysis. a–f, Dynamics of model population responses, same conventions as in Fig. 2. Responses are projected into the three-dimensional subspace spanned by the axes of choice, motion and colour (defined here based on the model synaptic weights, see Supplementary Information, section 7.6). Movement along the choice axis corresponds to integration of evidence, and the motion and colour inputs deflect the trajectories along the corresponding input axes. Fixed points of the dynamics (red crosses) were computed separately for motion (**a–c**) and colour contexts (**d–f**) in the absence of sensory inputs (see Supplementary Information, section 7.5). The fixed points are 'marginally stable' (that is, one eigenvalue of the linearized dynamics is close to zero, whereas all others have strongly negative real parts; see Supplementary Information). The locally computed right zero-eigenvectors (red lines) point to the neighbouring fixed points, which thus approximate a line attractor in each context. After the inputs are turned off (dots off, purple data points and lines) the responses relax back towards the line attractor. Each line attractor ends in two 'stable' attractors (that is, all eigenvalues have strongly negative real parts, large crosses) corresponding to model outputs of +1 and −1 (that is, choice 1 or 2).

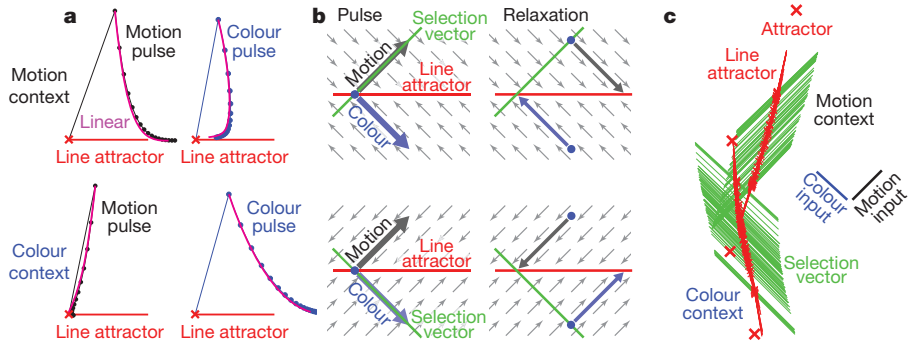

Figure 6 | Selection and integration by recurrent dynamics. **a**, Average model population response to short (1-ms) pulses of motion (left) and colour inputs (right) during motion (top) and colour contexts (bottom). Motion or colour inputs (solid lines) are initiated when the system is steady at one of the identified fixed points (red crosses), and subsequent relaxation back to the line attractor is simulated (dots: 3-ms intervals) and averaged across fixed points. The size of the pulses approximately corresponds to the length of the scale bars in Fig. 5. Selection of the relevant input results from the context-dependent relaxation of the recurrent dynamics after the pulse, and is well approximated by the linearized dynamics around the fixed points (magenta lines). Responses are projected into the two-dimensional subspace spanned by the direction of the pulse and the locally computed line attractor (the right zero-eigenvector of the linearized dynamics). **b**, Explanation of how the same input pulse (left) leads to evidence integration in one context, but is ignored in the other (right). Relaxation towards the line attractor (small arrows) is always orthogonal to the context-dependent selection vector, and reverses the effects of the irrelevant pulse. **c**, Global arrangement of the line attractor (red) and selection vector (green) at each fixed point. Inputs are selected by the selection vector, which is orthogonal to the contextually irrelevant input (note input axes, right), and integrated along the line attractor.

dynamics, although counterintuitive, nevertheless follow a very simple rule. For a given context, the relaxation always occurs on a path that is orthogonal to a specific direction in state space, which we call the 'selection vector' (Fig. 6b). The direction of the selection vector, like the direction of the line attractor, is a property of the recurrent synaptic weights learned by the model during training (see Supplementary Information). Unlike the line attractor, however, the orientation of the selection vector changes with context—it projects strongly onto the relevant input, but is orthogonal to the irrelevant one (Fig. 6b). As a consequence, the relaxation dynamics around the line attractor are context dependent. This mechanism explains how the same sensory input can result in movement along the line attractor in one context but not the other (Fig. 6b).

The line attractor and the selection vector are sufficient to explain the linearized dynamics around each fixed point (see Supplementary Information), and approximate well the responses of the full model (magenta curves, Fig. 6a). Mathematically, the line attractor and the selection vector correspond to the right and left zero-eigenvector of the underlying linear system. Within a context, these locally defined eigenvectors point in a remarkably consistent direction across different fixed points—the selection vector, in particular, is always aligned with the relevant input and orthogonal to the irrelevant input (Fig. 6c and Extended Data Fig. 10q–s). As a result, the two line attractors (Fig. 6c) show relaxation dynamics appropriate for selecting the relevant input along their entire length.

Discussion

We describe a novel mechanism underlying flexible, context-dependent selection of sensory inputs and their integration towards a choice (see refs 39–41 for related concepts). This mechanism is sufficient to explain the selection and integration of motion inputs in both monkeys, and of colour inputs in monkey A, which are not filtered out by context before they reach PFC.

A randomly initialized, recurrent neural network trained to solve a task analogous to the monkeys' task reproduces the main features of the data, and analysis of the trained network elucidates the novel selection mechanism. Integration along line attractors, and its relation to the selection vector, has been described before[39]. However, our model demonstrates how a single nonlinear model can implement flexible computations by reconfiguring the selection vector and the corresponding recurrent dynamics based on a contextual input. Counterintuitively, in the model the projection of an input onto the line attractor does not determine the extent to which it is integrated, a manifestation of 'non-normal' dynamics[40,42,43] (see Supplementary Information).

Our results show that the modulation of sensory responses is not necessary to select among sensory inputs (see also refs 44–46). Consistent with this conclusion, two studies using tasks similar to ours[47,48], as well as our own recordings in the middle temporal visual area (MT) of monkey A (data not shown), have found no evidence for consistent firing rate modulations in the relevant sensory areas. The dynamical process outlined in this paper is fully sufficient for context-dependent selection in a variety of behavioural models[3–8], but it need not be exclusive. Multiple selection mechanisms may exist within the brain.

Our results indicate that computations in prefrontal cortex emerge from the concerted dynamics of large populations of neurons, and are well studied in the framework of dynamical systems[17,19–23,24,39,49]. Notably, the rich dynamics of PFC responses during selection and integration of inputs can be characterized and understood with just two features of a dynamical system—the line attractor and the selection vector, which are defined only at the level of the neural population. This parsimonious account of cortical dynamics contrasts markedly with the complexity of single neuron responses typically observed in PFC and other integrative structures, which reveal multiplexed representation of many task-relevant and choice-related signals[1,2,15,16,25,26,50]. In light of our results, these mixtures of signals can be interpreted as separable representations at the level of the neural population[15,17,25,26]. A fundamental function of PFC may be to generate such separable representations, and to flexibly link them through appropriate recurrent dynamics to generate the desired behavioural outputs.

METHODS SUMMARY

Two adult male rhesus monkeys (14 and 12 kg) were trained on a two-alternative, forced-choice, visual discrimination task. While the monkeys were engaged in the behavioural task, we recorded single- and multiunit responses in the arcuate sulcus and the prearcuate gyrus, and in cortex near and lateral to the principal sulcus. The great majority of neurons were not recorded simultaneously, but rather in separate behavioural sessions. All surgical and behavioural procedures conformed to the guidelines established by the National Institutes of Health and were approved by the Institutional Animal Care and Use Committee of Stanford University. We pooled data from single- and multiunit recordings to construct population responses, and used state space analysis to study the effect of task conditions and time on the population responses. We developed a dimensionality reduction technique ('targeted dimensionality reduction') to identify a low-dimensional subspace capturing variance due to the task variables of interest. We compared the recorded responses to the responses of units in a nonlinear, recurrent neural network model. We trained the model (that is, optimized its

synaptic weights with a 'back-propagation' algorithm) to perform a task analogous to the one performed by the monkeys. We then reverse-engineered the model to discover its mechanism of selective integration. We identified fixed points of the model dynamics, linearized the dynamics around the fixed points, and used linear systems analysis to understand the linearized dynamics. Full methods are provided in the Supplementary Information.

Online Content Any additional Methods, Extended Data display items and Source Data are available in the online version of the paper; references unique to these sections appear only in the online paper.

Received 27 September 2012; accepted 8 October 2013.

1. Fuster, J. M. *The Prefrontal Cortex* 4th edn (Academic, 2008).
2. Miller, E. K. & Cohen, J. D. An integrative theory of prefrontal cortex function. *Annu. Rev. Neurosci.* **24,** 167–202 (2001).
3. Desimone, R. & Duncan, J. Neural mechanisms of selective visual attention. *Annu. Rev. Neurosci.* **18,** 193–222 (1995).
4. Schroeder, C. E. & Lakatos, P. Low-frequency neuronal oscillations as instruments of sensory selection. *Trends Neurosci.* **32,** 9–18 (2009).
5. Noudoost, B., Chang, M. H., Steinmetz, N. A. & Moore, T. Top-down control of visual attention. *Curr. Opin. Neurobiol.* **20,** 183–190 (2010).
6. Reynolds, J. H. & Chelazzi, L. Attentional modulation of visual processing. *Annu. Rev. Neurosci.* **27,** 611–647 (2004).
7. Maunsell, J. H. & Treue, S. Feature-based attention in visual cortex. *Trends Neurosci.* **29,** 317–322 (2006).
8. Fries, P. Neuronal gamma-band synchronization as a fundamental process in cortical computation. *Annu. Rev. Neurosci.* **32,** 209–224 (2009).
9. Mansouri, F. A., Tanaka, K. & Buckley, M. J. Conflict-induced behavioural adjustment: a clue to the executive functions of the prefrontal cortex. *Nature Rev. Neurosci.* **10,** 141–152 (2009).
10. Tanji, J. & Hoshi, E. Role of the lateral prefrontal cortex in executive behavioral control. *Physiol. Rev.* **88,** 37–57 (2008).
11. Bruce, C. J. & Goldberg, M. E. Primate frontal eye fields. I. Single neurons discharging before saccades. *J. Neurophysiol.* **53,** 603–635 (1985).
12. Schall, J. D. The neural selection and control of saccades by the frontal eye field. *Phil. Trans. R. Soc. Lond. B* **357,** 1073–1082 (2002).
13. Moore, T. The neurobiology of visual attention: finding sources. *Curr. Opin. Neurobiol.* **16,** 159–165 (2006).
14. Kim, J. N. & Shadlen, M. N. Neural correlates of a decision in the dorsolateral prefrontal cortex of the macaque. *Nature Neurosci.* **2,** 176–185 (1999).
15. Machens, C. K., Romo, R. & Brody, C. D. Functional, but not anatomical, separation of ''what'' and ''when'' in prefrontal cortex. *J. Neurosci.* **30,** 350–360 (2010).
16. Rigotti, M. *et al.* The importance of mixed selectivity in complex cognitive tasks. *Nature* **497,** 585–590 (2013).
17. Stokes, M. G. *et al.* Dynamic coding for cognitive control in prefrontal cortex. *Neuron* **78,** 364–375 (2013).
18. Hernández, A. *et al.* Decoding a perceptual decision process across cortex. *Neuron* **66,** 300–314 (2010).
19. Churchland, M. M. *et al.* Neural population dynamics during reaching. *Nature* **487,** 51–56 (2012).
20. Shenoy, K. V., Sahani, M. & Churchland, M. M. Cortical control of arm movements: a dynamical systems perspective. *Annu. Rev. Neurosci.* **36,** 337–359 (2013).
21. Stopfer, M., Jayaraman, V. & Laurent, G. Intensity versus identity coding in an olfactory system. *Neuron* **39,** 991–1004 (2003).
22. Briggman, K. L., Abarbanel, H. D. & Kristan, W. B. Jr. Optical imaging of neuronal populations during decision-making. *Science* **307,** 896–901 (2005).
23. Harvey, C. D., Coen, P. & Tank, D. W. Choice-specific sequences in parietal cortex during a virtual-navigation decision task. *Nature* **484,** 62–68 (2012).
24. Afshar, A. *et al.* Single-trial neural correlates of arm movement preparation. *Neuron* **71,** 555–564 (2011).
25. Sigala, N., Kusunoki, M., Nimmo-Smith, I., Gaffan, D. & Duncan, J. Hierarchical coding for sequential task events in the monkey prefrontal cortex. *Proc. Natl Acad. Sci. USA* **105,** 11969–11974 (2008).
26. Machens, C. K. Demixing population activity in higher cortical areas. *Front. Comput. Neurosci.* **4,** 126 (2010).
27. Shadlen, M. N. & Newsome, W. T. Neural basis of a perceptual decision in the parietal cortex (area LIP) of the rhesus monkey. *J. Neurophysiol.* **86,** 1916–1936 (2001).
28. Mazurek, M. E., Roitman, J. D., Ditterich, J. & Shadlen, M. N. A role for neural integrators in perceptual decision making. *Cereb. Cortex* **13,** 1257–1269 (2003).
29. Wang, X. J. Probabilistic decision making by slow reverberation in cortical circuits. *Neuron* **36,** 955–968 (2002).
30. Cohen, J. D., Dunbar, K. & McClelland, J. L. On the control of automatic processes: a parallel distributed processing account of the Stroop effect. *Psychol. Rev.* **97,** 332–361 (1990).
31. Deco, G. & Rolls, E. T. Attention and working memory: a dynamical model of neuronal activity in the prefrontal cortex. *Eur. J. Neurosci.* **18,** 2374–2390 (2003).
32. Sussillo, D. & Abbott, L. F. Generating coherent patterns of activity from chaotic neural networks. *Neuron* **63,** 544–557 (2009).
33. Sussillo, D. & Barak, O. Opening the black box: low-dimensional dynamics in high-dimensional recurrent neural networks. *Neural Comput.* **25,** 626–649 (2013).
34. Zipser, D. & Andersen, R. A. A back-propagation programmed network that simulates response properties of a subset of posterior parietal neurons. *Nature* **331,** 679–684 (1988).
35. Martens, J. & Sutskever, I. Learning recurrent neural networks with hessian-free optimization. *Proc. 28th Int. Conf. Machine Learn.* (ICML, 2011).
36. Churchland, A. K., Kiani, R. & Shadlen, M. N. Decision-making with multiple alternatives. *Nature Neurosci.* **11,** 693–702 (2008).
37. Reddi, B. A. & Carpenter, R. H. The influence of urgency on decision time. *Nature Neurosci.* **3,** 827–830 (2000).
38. Brunton, B. W., Botvinick, M. M. & Brody, C. D. Rats and humans can optimally accumulate evidence for decision-making. *Science* **340,** 95–98 (2013).
39. Seung, H. S. How the brain keeps the eyes still. *Proc. Natl Acad. Sci. USA* **93,** 13339–13344 (1996).
40. Goldman, M. S. Memory without feedback in a neural network. *Neuron* **61,** 621–634 (2009).
41. Sejnowski, T. J. On the stochastic dynamics of neuronal interaction. *Biol. Cybern.* **22,** 203–211 (1976).
42. Murphy, B. K. & Miller, K. D. Balanced amplification: a new mechanism of selective amplification of neural activity patterns. *Neuron* **61,** 635–648 (2009).
43. Ganguli, S., Huh, D. & Sompolinsky, H. Memory traces in dynamical systems. *Proc. Natl Acad. Sci. USA* **105,** 18970–18975 (2008).
44. Salinas, E. Context-dependent selection of visuomotor maps. *BMC Neurosci.* **5,** 47 (2004).
45. Zénon, A. & Krauzlis, R. J. Attention deficits without cortical neuronal deficits. *Nature* **489,** 434–437 (2012).
46. Roy, J. E., Riesenhuber, M., Poggio, T. & Miller, E. K. Prefrontal cortex activity during flexible categorization. *J. Neurosci.* **30,** 8519–8528 (2010).
47. Sasaki, R. & Uka, T. Dynamic readout of behaviorally relevant signals from area MT during task switching. *Neuron* **62,** 147–157 (2009).
48. Katzner, S., Busse, L. & Treue, S. Attention to the color of a moving stimulus modulates motion-signal processing in macaque area MT: evidence for a unified attentional system. *Front. Syst. Neurosci.* **3,** 12 (2009).
49. Machens, C. K., Romo, R. & Brody, C. D. Flexible control of mutual inhibition: a neural model of two-interval discrimination. *Science* **307,** 1121–1124 (2005).
50. Huk, A. C. & Meister, M. L. Neural correlates and neural computations in posterior parietal cortex during perceptual decision-making. *Front. Integr. Neurosci.* **6,** 86 (2012).

Supplementary Information is available in the online version of the paper.

Acknowledgements We thank J. Powell, S. Fong and J. Brown for technical assistance, L. Abbott, for conversations on non-normal dynamics, and L. Stryer, S. Hohl, S. Ganguli, M. Sahani, R. Kiani, C. Moore and T. Bhattacharya for discussions. V.M. and W.T.N. were supported by HHMI and the Air Force Research Laboratory (FA9550-07-1-0537); D.S. and K.V.S. by an NIH Director's Pioneer Award (1DP1OD006409) and DARPA REPAIR (N66001-10-C-2010).

Author Contributions V.M. and W.T.N. designed the study. V.M. collected the data. D.S. implemented the recurrent network. V.M. and D.S. analysed and modelled the data. V.M., D.S., K.V.S. and W.T.N. discussed the findings and wrote the paper.

Author Information Reprints and permissions information is available at www.nature.com/reprints. The authors declare no competing financial interests. Readers are welcome to comment on the online version of the paper. Correspondence and requests for materials should be addressed to V.M. (valerio@ini.phys.ethz.ch) or D.S. (sussillo@stanford.edu).

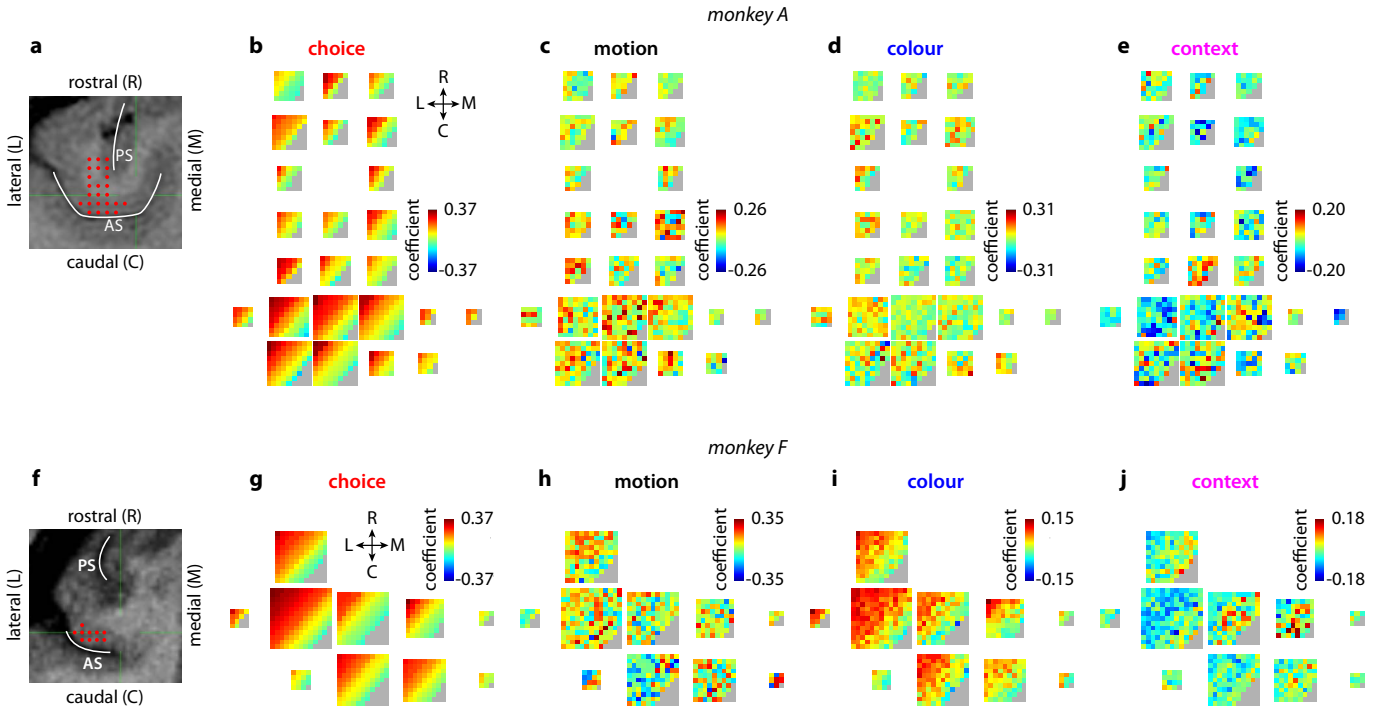

Extended Data Figure 1 | Recording locations and task-related patterns of population activity in PFC. **a**, Recording locations (red dots) in monkey A are shown on anatomical magnetic resonance images in imaging planes that were oriented perpendicularly to the direction of electrode penetrations. Electrodes were lowered through a grid (1-mm spacing) positioned over the arcuate sulcus (AS). Recordings covered the entire depth of the AS and extended rostrally onto the prearcuate gyrus and cortex near and lateral to the principal sulcus (PS). **b**–**e**, Representation of four task variables in the population response. Each multi-coloured square corresponds to a recording location (red dots) in **a**. Within each square, each pixel corresponds to a unit recorded from that grid position, such that each square represents all the units recorded at the corresponding location. The colour of a pixel indicates the de-noised regression coefficient of choice (**b**), motion coherence (**c**), colour coherence (**d**) and context (**e**) for a given unit (colour bars; grey: no units). These coefficients describe how much the trial-by-trial firing rate of a given unit depends on the task variables in **b**–**e**. The position of each unit within a square is arbitrary; we therefore sorted them according to the amplitude of the coefficient of choice, which accounts for the diagonal bands of colour in **b** (top-left to bottom-right, high to low choice coefficient). The positions of the pixels established in **b** are maintained in **c**–**e**, so that one can compare the amplitude of the coefficient for each task variable for every unit recorded from monkey A. Each of the four panels can be interpreted as the pattern of population activity elicited by the corresponding task variable. The four task variables elicit very distinct patterns of activity and are separable at the level of the population. Importantly, the coefficients were de-noised with principal component analysis (see Supplementary Information, section 6.7) and can be estimated reliably from noisy neural responses (Extended Data Fig. 4i–l). Differences between activation patterns therefore reflect differences in the properties of the underlying units, not noise. **f**–**j**, Recording locations and task-related patterns of population activity for monkey F. Same conventions as in **a**–**e**. Recordings (**f**) covered the entire depth of the AS. The patterns of population activity elicited by a choice (**g**), by the motion evidence (**h**) and by context (**j**) are distinct, meaning that the representations of these task variables are separable at the level of the population. The representations of choice (**g**) and colour (**i**), however, are not separable in monkey F, indicating that colour inputs are processed differently in the two monkeys (see main text).

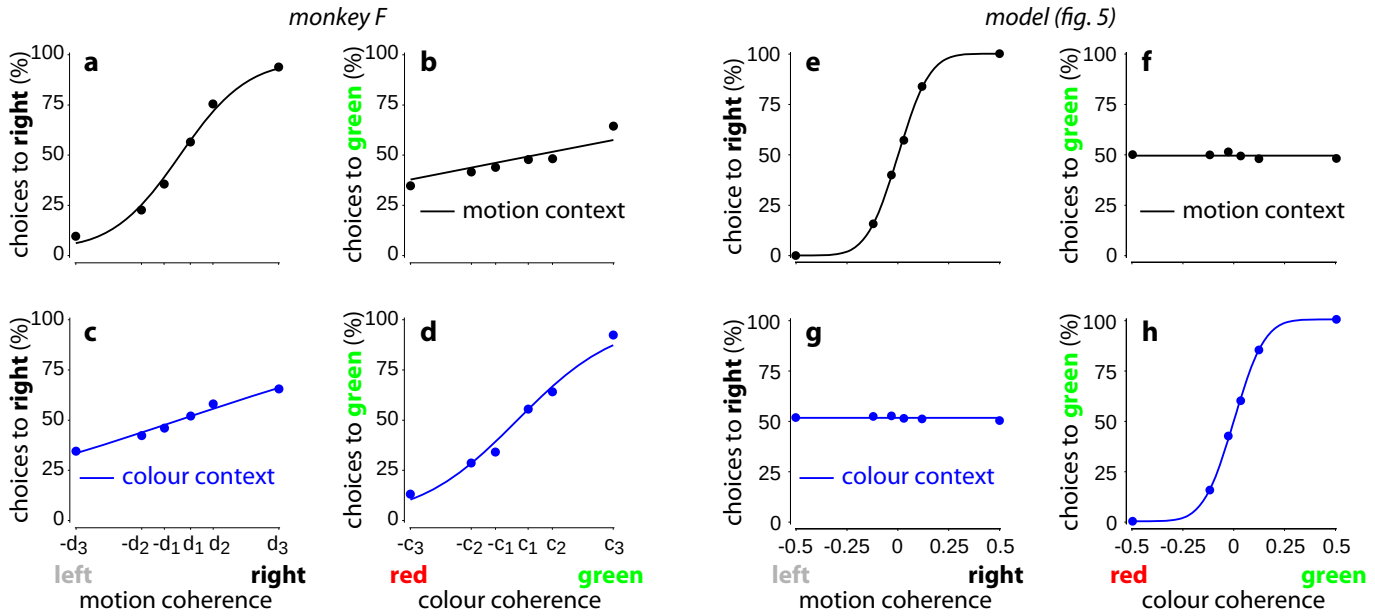

Extended Data Figure 2 | Psychophysical performance for monkey F and for the model. **a**–**d**, Psychophysical performance for monkey F, for motion (top) and colour contexts (bottom), averaged over 60 recording sessions (123,550 trials). Performance is shown as a function of motion (left) or colour (right) coherence in each behavioural context. As in Fig. 1c–f, coherence values along the horizontal axis correspond to the average low, intermediate and high motion coherence (**a**, **c**) and colour coherence (**b**, **d**) computed over all behavioural trials. The curves are fits of a behavioural model (see Supplementary Information, section 4). **e**–**h**, 'Psychophysical' performance for the trained neural-network model (Figs 4–6) averaged over a total of 14,400 trials (200 repetitions per condition). Choices were generated based on the output of the model at the end of the stimulus presentation—an output larger than zero corresponds to a choice to the left target (choice 1), and an output smaller than zero corresponds to a choice to the left target (choice 2). We simulated model responses to inputs with motion and colour coherences of 0.03, 0.12 and 0.50. The variability in the input (that is, the variance of the underlying Gaussian distribution) was chosen such that the performance of the model for the relevant sensory signal qualitatively matches the performance of the monkeys. As in Fig. 1c–f, performance is shown as a function of motion (left) or colour (right) coherence in the motion (top) and colour contexts (bottom). Curves are fits of a behavioural model (as in **a**–**d** and in Fig. 1c–f). In each behavioural context, the relevant sensory input affects the model's choices (**e**, **h**), but the irrelevant input does not (**f**, **g**), reflecting successful context-dependent integration. The model output essentially corresponds to the bounded temporal integral of the relevant input (not shown) and is completely unaffected by the irrelevant input.

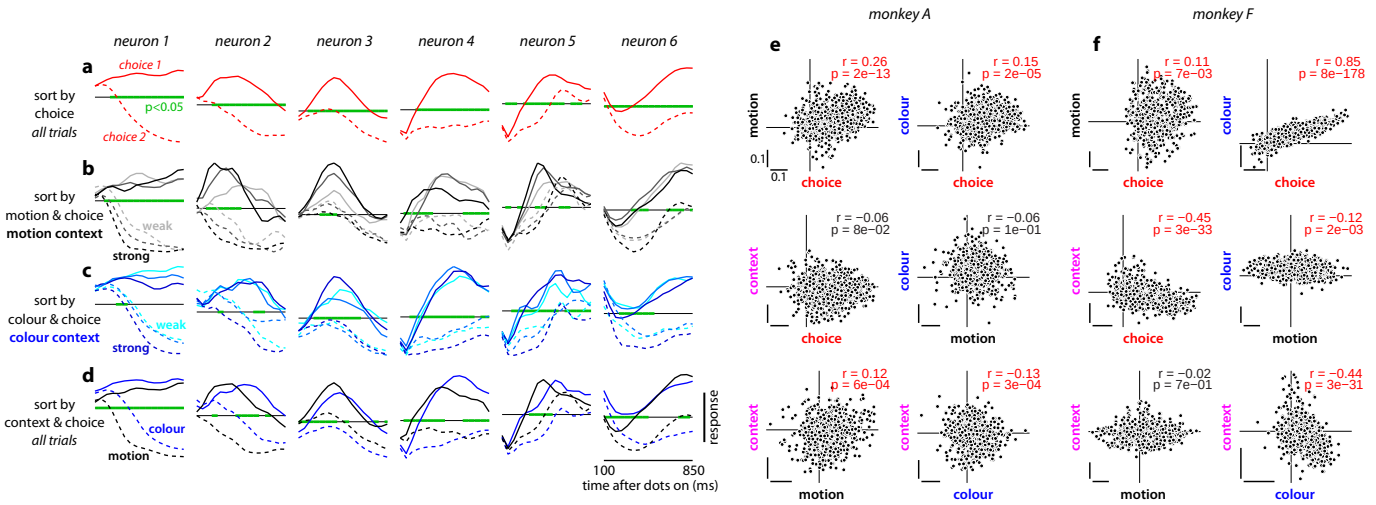

Extended Data Figure 3 | Mixed representation of task variables in PFC. **a**–**d**, Example responses from six well-isolated single units in monkey A. Each column shows average normalized responses on correct trials for one of the single units. Responses are aligned to the onset of the random-dot stimulus, averaged with a 50-ms sliding window, and sorted by one or more task-related variables (choice, motion coherence, colour coherence, context). The green lines mark time intervals with significant effects of choice (**a**), motion coherence (**b**), colour coherence (**c**), or context (**d**) as assessed by multi-variable, linear regression (regression coefficient different from zero, $P < 0.05$). Linear regression and coefficient significance are computed over all trials (correct and incorrect, motion and colour context; Supplementary Information, section 6.3). The horizontal grey line corresponds to a normalized response equal to zero. **a**, Responses sorted by choice (solid, choice 1; dashed, choice 2) averaged over both contexts. **b**, Responses during motion context, sorted by choice and motion coherence (black to light-grey, high to low motion coherence). **c**, Responses during colour context, sorted by choice and colour coherence (blue to cyan, high to low colour coherence). **d**, Responses sorted by choice and context (black, motion context; blue, colour context). As is typical for PFC, the activity of the example units depends on many task variables, indicating that they represent mixtures of the underlying task variables. **e**, **f**, De-noised regression coefficients for all units in monkey A (**e**) and monkey F (**f**). The data in Extended Data Fig. 1 are re-plotted here to directly compare the effects of different task variables (choice, motion, colour, context) to each other. Each data point corresponds to a unit, and the position along the horizontal and vertical axes is the de-noised regression coefficient for the corresponding task variable. The horizontal and vertical lines in each panel intersect at the origin (0,0). Scale bars span the same range (0.1) in each panel. The different task variables are mixed at the level of individual units. Although units modulated by only one of the task variables do occur in the population, they do not form distinct clusters but rather are part of a continuum that typically includes all possible combinations of selectivities. Significant correlations between coefficients are shown in red ($P < 0.05$, Pearson's correlation coefficient r).

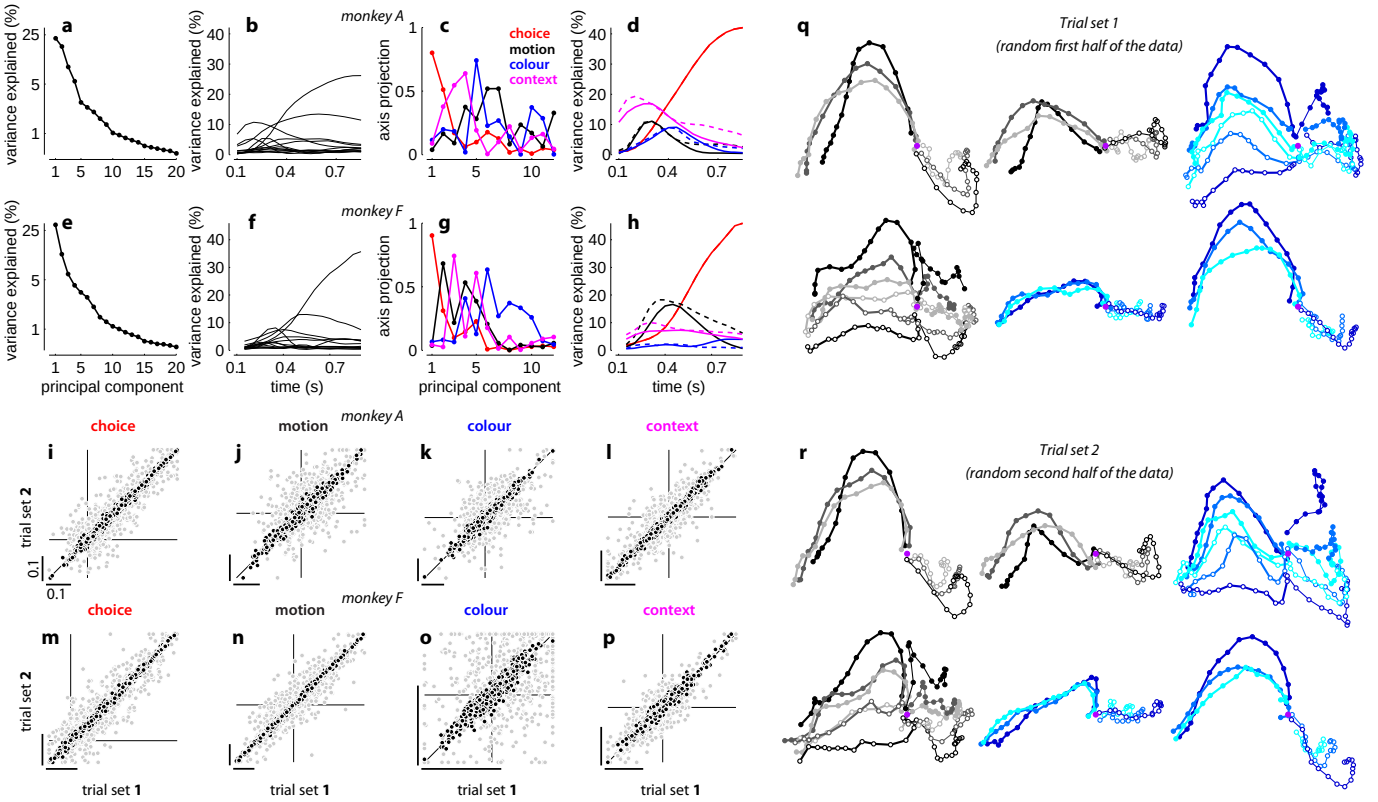

Extended Data Figure 4 | Targeted dimensionality reduction of population responses, and reliability of task-related axes and population trajectories. **a**, Fraction of variance explained by the first 20 principal components of the responses in monkey A. Principal components are computed on correct trials only, on condition-averaged responses. Conditions are defined on the basis of choice, motion coherence, colour coherence and context. Each time point of the average response for a given condition contributes an 'independent' sample for the principal components analysis, and variance is computed over conditions and times. **b**, Fraction of variance explained by the first 12 principal components. The total explainable variance (100%) is computed separately at each time, and reflects response differences across conditions. **c**, The four 'task-related axes' of choice, motion, colour and context expressed as linear combinations of the first 12 principal components. The four axes span a subspace containing the task-related variance in the population response (for example, Fig. 2 and Extended Data Fig. 6) and are obtained by orthogonalizing the de-noised regression vectors for the corresponding task variables (see Supplementary Information, section 6.7; de-noised regression coefficients are shown in Extended Data Figs 1 and 3e, f). The vertical axis in **c** corresponds to the projection of each axis onto a given principal component (that is, the contribution of that principal component to each axis). All four axes project onto multiple principal components and thus the corresponding task variables are mixed at the level of single principal components. **d**, Fraction of variance explained by the task-related axes of choice, motion, colour and context (solid lines), as in **b**. The four axes explain a larger fraction of the variance than the principal components at many times but, unlike the principal components, they do not explain the variance common to all conditions that is due to the passage of time (not shown). A possible concern with our analysis is that the time courses of variance explained in **d** could be misleading if the task-related axes, which we estimated only at a single time for each variable, are changing over time during the presentation of the random dots. Under this scenario, for example, the 'humped' shape of the motion input (solid black trace) might reflect a changing ensemble code for motion rather than actual changes in the strength of the motion signal in the neural population. To control for this possibility, we also computed time-varying 'task-related axes' by estimating the axes of motion, colour and context separately at each time throughout the 750-ms dots presentation. The fractions of variance explained by the time-varying axes (dashed lines) and by the fixed axes (solid lines) have similar amplitudes and time courses. Thus, the effects of the corresponding task variables (during the presentation of the random dots) are adequately captured by the subspace spanned by the fixed axes (see Supplementary Information, section 6.8). **e**–**h**, Same as **a**–**d**, for monkey F. As shown in Extended Data Figs 1g, i and 3f (top-right panel) the de-noised regression coefficients of colour and choice are strongly correlated. As a consequence, the axis of colour explains only a small fraction of the variance in the population responses (**h**, blue; see main text). **i**–**l**, Reliability of task-related axes in monkey A. To determine to what extent variability (that is, noise) in single unit responses affects the task-related axes of choice, motion, colour and context (for example, Fig. 2 and Extended Data Fig. 6), we estimated each axis twice from two separate sets of trials (trial sets 1 and 2 in **i**–**l**). For each unit, we first assigned each trial to one of two subsets, and estimated de-noised regression coefficients for the task variables separately for the two subsets. We then obtained task-related axes by orthogonalizing the corresponding de-noised coefficients (see Supplementary Information, section 6.9). Here, the orthogonalized coefficients are computed both with (black) and without (grey) PCA-based de-noising. The horizontal and vertical lines in each panel intersect at the origin (0,0). Scale bars span the same range (0.1) in each panel. Data points lying outside the specified horizontal or vertical plotting ranges are shown on the corresponding edges in each panel. **i**, Coefficients of choice. Each data point corresponds to the orthogonalized coefficient of choice for a given unit, computed from trials in set 1 (horizontal axis) or in set 2 (vertical axis). **j**–**l**, Same as **i** for the orthogonalized coefficients of motion (**j**), colour (**k**) and context (**l**). **m**–**p**, Orthogonalized regression coefficients for monkey F, as in **i**–**l**. Overall, after de-noising the orthogonalized coefficients are highly consistent across the two sets of trials. Therefore, the observed differences in the activation pattern elicited by different task variables (Extended Data Fig. 1) are not due to the noisiness of neural responses, but rather reflect differences in the properties of the underlying units. **q**, **r**, Reliability of population trajectories. To assess the reliability of the trajectories in Fig. 2, we estimated the task-related axes and the resulting population trajectories (same conventions as Fig. 2) twice from two separate sets of trials (as **i**–**l**, see Supplementary Information, section 6.9). As in the example trajectories shown in **q** (trial set 1) and **r** (trial set 2), we consistently obtained very similar trajectories across the two sets of trials. To quantify the similarity between the trajectories from the two sets, we used trajectories obtained from one set to predict the trajectories obtained from the other set (see Supplementary Information, section 6.9). On average across 20 randomly defined pairs of trial sets, in both monkeys the population responses from one set explain 94% of the total variance in the responses of the other set (95% for the example in **q** and **r**). These numbers provide a lower bound on the true reliability of trajectories in Fig. 2, which are based on twice as many trials as those in **q** and **r**.

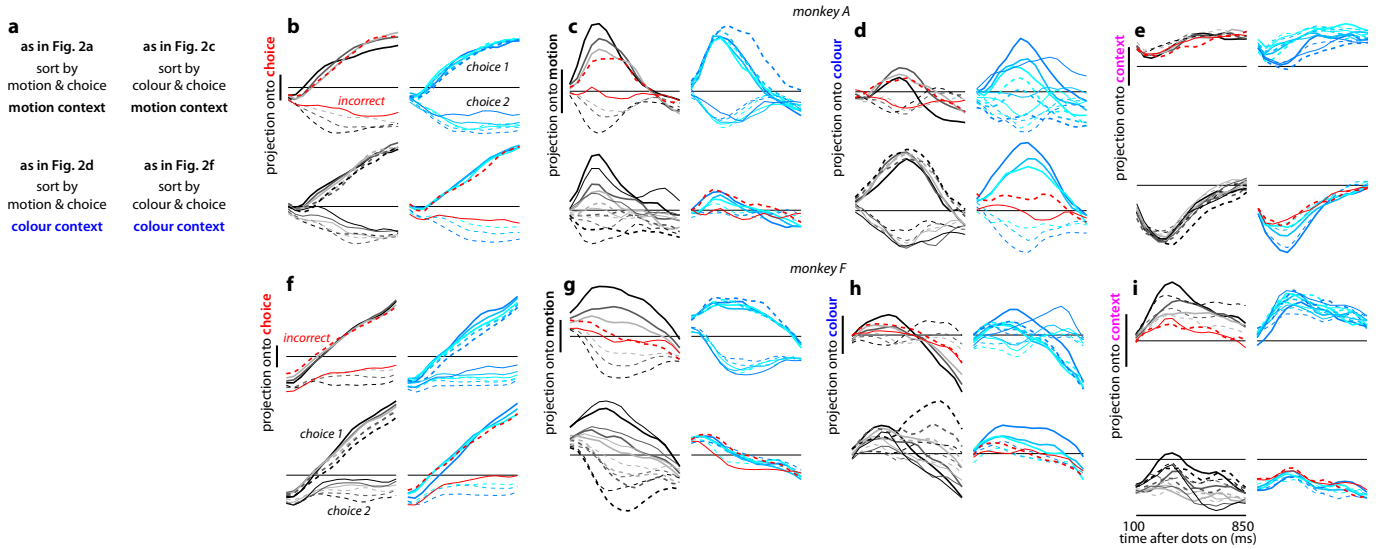

Extended Data Figure 5 | Population responses along individual task-related axes. **a**–**e**, Responses for monkey A. The average population responses on correct trials are re-plotted from Fig. 2, together with responses on a subset of incorrect trials (red curves). Here the responses are represented explicitly as a function of time (horizontal axis) and projected separately (vertical axes) onto the axes of choice (**b**), motion (**c**), colour (**d**) and context (**e**). As in Fig. 2, correct trials are sorted on the basis of context (motion: top sub-panels; colour: bottom sub-panels; see key in **a**), on the direction of the sensory evidence (filled, towards choice 1; dashed, towards choice 2) and strength of the sensory evidence (black to light-grey, strongest to weakest motion; blue to cyan, strongest to weakest colour), and based on choice (thick, choice 1; thin, choice 2). Incorrect trials (red curves) are shown for the lowest motion coherence (during motion context, top left in **b**–**e**) and the lowest colour coherence (during colour context, bottom right in **b**–**e**). Vertical scale bars correspond to 1 unit of normalized response, and the horizontal lines are drawn at the same level in all four sub-panels within **b**–**e**. **a**, Key to the condition averages shown in each panel of **b**–**e**, as well as to the corresponding state-space panels in Fig. 2. **b**, Projections of the population response onto the choice axis. Responses along the choice axis represent integration of evidence in both contexts. **c**, Projection onto the motion axis. Responses along the motion axis represent the momentary motion evidence during both motion (top left) and colour contexts (bottom left) (curves are parametrically ordered based on motion strength in both contexts), but not the colour evidence (right, curves are not ordered based on colour strength). **d**, Projection onto the colour axis. Responses along the colour axis represent the momentary colour evidence in the motion (top right) and colour contexts (bottom right) (ordered), but not the motion evidence (left, not ordered). **e**, Projection onto the context axis. Responses in the motion context (top, all curves above the horizontal line) and colour context (bottom, all curves below the horizontal line) are separated along the context axis, which maintains a representation of context. **f**–**i**, Responses for monkey F, same conventions as in **b**–**e**. The responses in **f**–**i** are also shown as trajectories in Extended Data Fig. 7g–l. The drift along the choice axis in Extended Data Fig. 7g–l is reflected in the overall positive slopes in **f**.

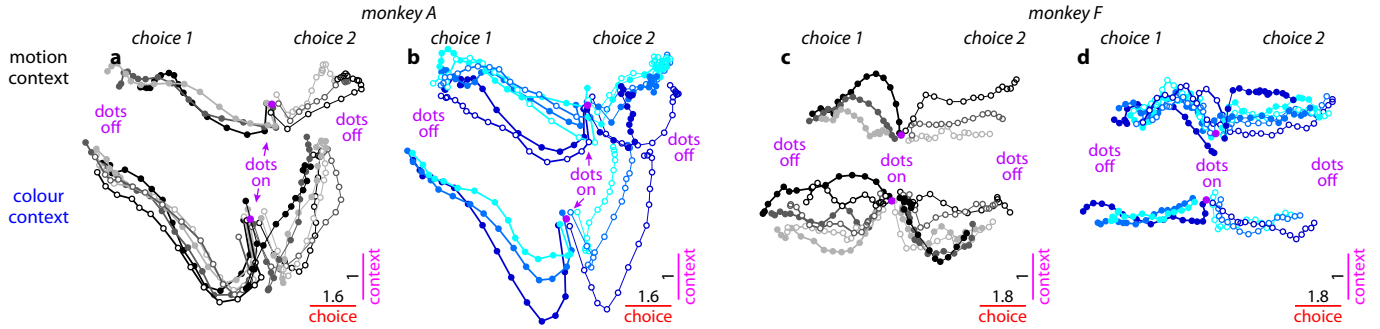

Extended Data Figure 6 | Effect of context on PFC dynamics. **a**, **b**, Responses from monkey A. Same conditions and conventions as in Fig. 2, but for activity projected into the two-dimensional subspace capturing the variance due to choice (along the choice axis) and context (context axis). Components along the choice axis are enhanced relative to the context axis (see scale bars). The population response contains a representation of context, which is reflected in the separation between trajectories in the motion and colour contexts along the axis of context. The contextual signal is strongest early during the dots presentation. **a**, Effects of context (motion context versus colour context), choice (choice 1 versus choice 2), and motion input (direction and coherence, grey colours). **b**, Same trials as in **a**, but averaged to show the effect of the colour input (blue colours). **c**, **d**, Responses from monkey F, same conventions as in **a**, **b**. As in Extended Data Fig. 7a–f, we subtracted the across-condition average trajectory from each individual, raw trajectory (see Supplementary Information, section 6.10). The underlying raw population responses are shown in Extended Data Fig. 5f–i, and confirm that the representation of context is stable throughout the dots presentation time (Extended Data Fig. 5i).

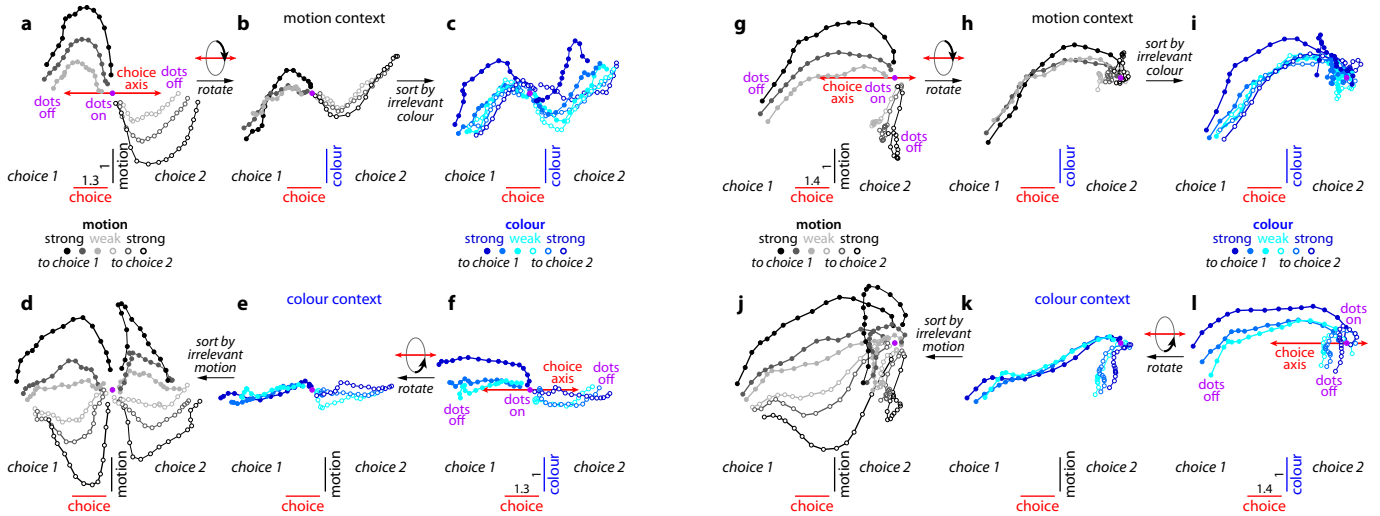

Extended Data Figure 7 | Dynamics of population responses in monkey F. **a**–**f**, Response trajectories in the subspace spanned by the task-related axes of choice, motion and colour. Same conventions as in Fig. 2. Unlike in Fig. 2, here we subtracted the across-condition average trajectory from each individual, raw trajectory (see Supplementary Information, section 6.10). The raw trajectories are shown in **g**–**l** and the corresponding projections onto individual axes in Extended Data Fig. 5f–i. Three key features of the population responses are shared in monkey A (Fig. 2) and monkey F. First, movement along a single choice axis (**a** and **f**, red arrows) corresponds to integration of the relevant evidence in both contexts. Second, in both contexts the momentary motion evidence elicits responses along the axis of motion, which is substantially different from the axis of choice (**a** and **d**). Third, the motion evidence is strongly represented whether it is relevant (**a**) or irrelevant (**d**). Thus, the processing of motion inputs in both monkeys is inconsistent with current models of selection and integration (Fig. 3b–d). Unlike in monkey A, responses along the colour axis in monkey F (**f** and **c**) reflect the momentary colour evidence only weakly. The effects of colour on the trajectories in monkey F resemble the responses expected by the early selection model (Fig. 3b). **g**–**l**, Raw population responses. Population trajectories were computed and are represented as in Fig. 2. The trajectories in **a**–**f** were obtained by subtracting the across-condition average from each individual trajectory shown above. Overall, the responses have a tendency to move towards the left along the choice axis. An analogous, although weaker, overall drift can also be observed in monkey A, and contributes to the asymmetry between trajectories on choice 1 and choice 2 trials (Fig. 2). Because choice 1 corresponds to the target in the response field of the recorded neurons (see Supplementary Information, section 6.2), the drift reflects a tendency of individual firing rates to increase throughout the stimulus presentation time. By the definition of choice 1 and choice 2, a similar but opposite drift has to occur in neurons whose response field overlaps with choice 2 (the responses of which we did not record). In the framework of diffusion-to-bound models, such a drift can be interpreted as an urgency signal, which guarantees that the decision boundary is reached before the offset of the dots (refs 36, 37).

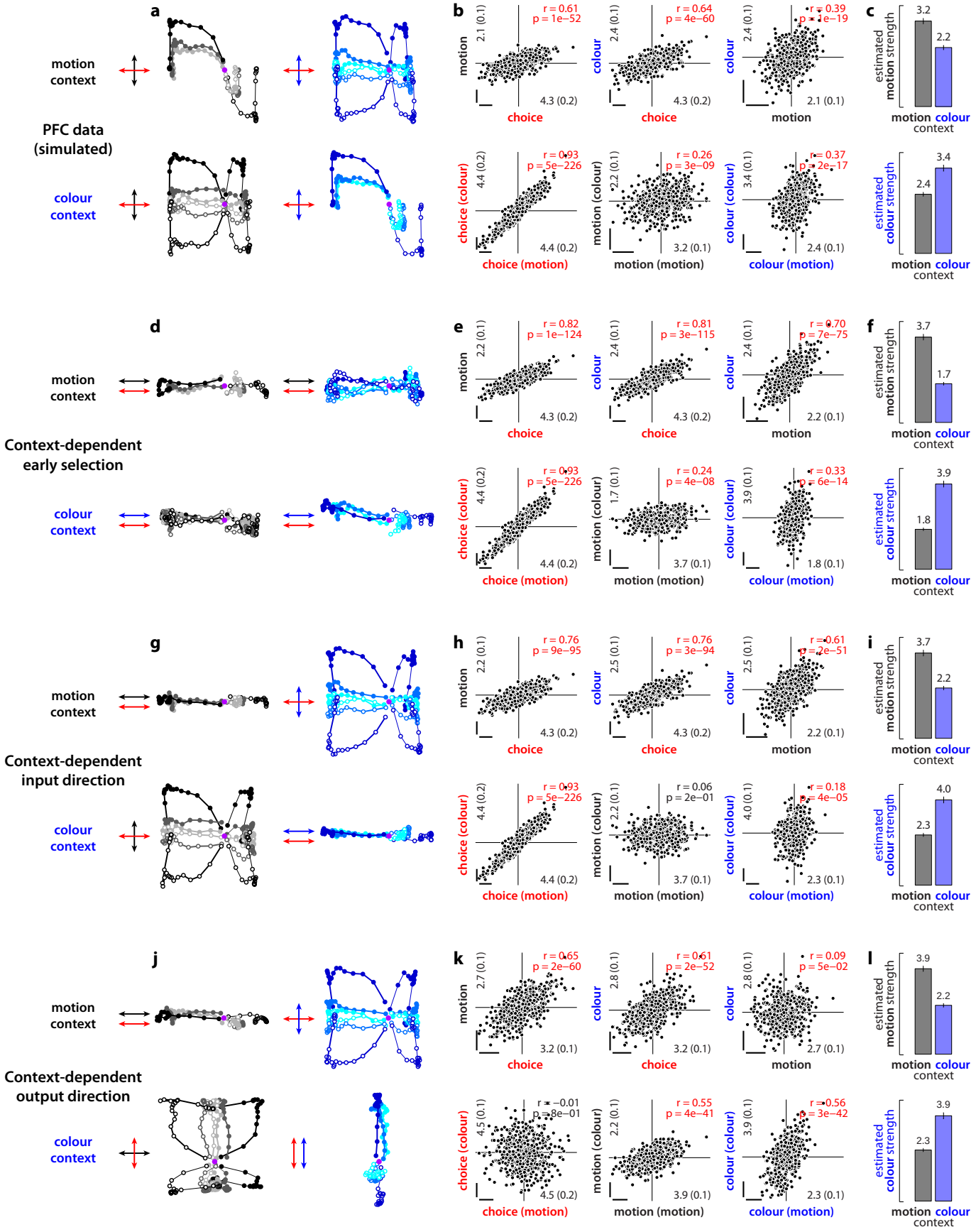

Extended Data Figure 8 | Simulations of models of selective integration inconsistent with PFC responses. We simulated population responses mimicking the observed PFC responses (**a**–**c**) and alternative responses expected based on the three models of context-dependent selection described in Fig. 3b–d (**d**–**l**) (see Supplementary Information, section 8). These simulations are based on a diffusion-to-bound model, unlike the simulations of the recurrent neural network models in Figs 5 and 6 and in Extended Data Figs 9 and 10e–s. Here, single neurons represent mixtures of three time-dependent task variables of a diffusion-to-bound model, namely the momentary motion and colour evidence and the integrated relevant evidence. At the level of the population, these three task variables are represented along specific directions in state space (arrows in **a**, **d**, **g**, **j**; red, integrated evidence; black, momentary motion evidence; blue, momentary colour evidence). The four simulations differ only with respect to the direction and context dependence of the three task variables. We computed state space trajectories from the population responses using the targeted dimensionality reduction techniques discussed in the main text and in Supplementary Information. The resulting simulated population responses reproduce the schematic population responses in Fig. 3. **a**–**c**, Simulated population responses mimicking the observed PFC responses (Fig. 2). **a**, Response trajectories in the two-dimensional subspace capturing the effects of choice and motion (left) or choice and colour (right) in the motion (top) and colour (bottom) contexts. Same conditions and conventions as in Fig. 2a, c and Fig. 2d, f. The three task variables are represented along three orthogonal directions in state space (arrows). **b**, Regression coefficients of choice, motion and colour for all simulated units in the population. For each unit, coefficients were computed with linear regression on all simulated trials (top) or separately on trials from the motion or colour context (bottom, context in parentheses). Scale bars represent arbitrary units. Numbers in the inset along each axis represent averages of the absolute value of the corresponding coefficients (±s.e.m., in parentheses). Significant correlations between coefficients are shown in red ($P < 0.05$, Pearson's correlation coefficient r. **c**, Estimated strengths of the motion (top) and colour (bottom) inputs during motion (black) and colour (blue) contexts. Input strength is defined as the average of the absolute value of the corresponding regression coefficients. **d**–**f**, same as **a**–**c**, for simulated population responses expected from context-dependent early selection (Fig. 3b). When relevant, momentary motion (top) and colour (bottom) evidence are represented along the same direction as integrated evidence (arrows in **d**). **g**–**i**, same as **a**–**c**, for simulated population responses expected from context-dependent input directions (Fig. 3c). Integrated evidence is represented along the same direction in both contexts (red arrows in **g**). The relevant momentary evidence (motion in the motion context, top; colour in the colour context, bottom) is aligned with the direction of integration, whereas the irrelevant momentary evidence is orthogonal to it (black and blue arrows in **g**). **j**–**l**, same as **a**–**c**, for simulated population responses expected from context-dependent output directions (Fig. 3d). The momentary motion and colour evidence are represented along the same directions in both contexts (black and blue arrows in **j**). The direction of integration (red arrows in **j**) is aligned with the motion evidence in the motion context (top), and with the colour evidence in the colour context (bottom).

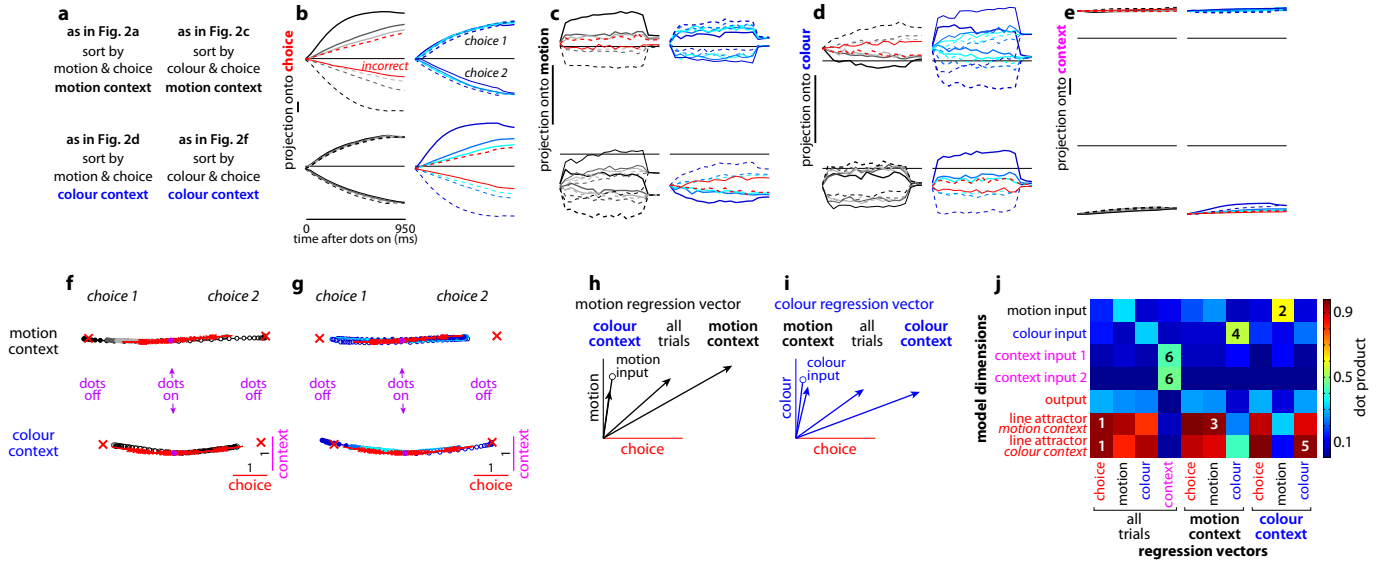

Extended Data Figure 9 | Model population responses and validation of targeted dimensionality reduction. **a**–**e**, Model population responses along individual task-related axes, same conventions as in Extended Data Fig. 5. Here we defined the task-related axes directly based on the synaptic connectivity in the model (see Supplementary Information, section 7.6; and panels **h**–**j**), rather than using the approximate estimates based on the population response (as for the PFC data, for example, Fig. 2). The same axes and the resulting projections underlie the trajectories in Fig. 5. The model integrates the contextually relevant evidence almost perfectly, and the responses along the choice axis (**b**) closely match the output of an appropriately tuned diffusion-to-bound model (not shown). Notably, near-perfect integration is not a core feature of the proposed mechanism of context-dependent selection (see main text, and Extended Data Fig. 10). **f**, **g**, Effect of context on model dynamics, same conditions and conventions as in Extended Data Fig. 6. Network activity is projected onto the two-dimensional subspace capturing the variance due to choice (along the choice axis) and context (context axis). Same units on both axes (see scale bars). As in Fig. 5, fixed points of the dynamics (red crosses) and the associated right zero-eigenvectors (that is, the local direction of the line attractor, red lines) were computed separately for motion (top) and colour contexts (bottom) in the absence of sensory inputs. The line attractors computed in the two contexts, and the corresponding population trajectories, are separated along the context axis. **f**, Effects of context (motion context, colour context), choice (choice 1, choice 2) and motion input (direction and coherence, grey colours) on the population trajectories. **g**, Same trials as in **f**, but re-sorted and averaged to show the effect of the colour input (blue colours). The context axis is approximately orthogonal to the motion and colour inputs, and thus the effects of motion and colour on the population response (Fig. 5) are not revealed in the subspace spanned by the choice and context axes (**f** and **g**). **h**–**j**, Validation of targeted dimensionality reduction. To validate the dimensionality reduction approach used to analyse population responses in PFC (see Supplementary Information, sections 6.5–6.7), we estimated the regression vectors of choice, motion, colour and context from the simulated population responses (Fig. 5 and panels **b**–**g**) and compared them to the exactly known model dimensions that underlie the model dynamics (see definitions below). We estimated the regression vectors in three ways: by pooling responses from all model units and all trials (as in the PFC data, for example, Fig. 2 and Extended Data Fig. 6), or separately from the motion- and colour-relevant trials (contexts). Orthogonalization of the regression vectors yields the task-related axes of the subspace of interest (for example, axes in Fig. 2). Most model dimensions (motion, colour and context inputs, and output) were defined by the corresponding synaptic weights after training. The line attractor, on the other hand, is the average direction of the right zero-eigenvector of the linearized dynamics around a fixed point, and was computed separately for the motion and colour contexts. **h**, The three regression vectors of motion (black arrows), plotted in the subspace spanned by the choice axis (that is, the regression vector of choice) and the motion axis (that is, the component of the regression vector of motion orthogonal to the choice axis). In the colour context, the motion regression vector closely approximates the actual motion input (black circle—the model dimension defined by synaptic weights). During the motion context, however, the motion regression vector has a strong component along the choice axis, reflecting the integration of motion evidence along that axis. The motion regression vector estimated from all trials corresponds to the average of the vectors from the two contexts; thus all three motion regression vectors lie in the same plane. **i**, The three regression vectors of colour (blue arrows) plotted in the subspace spanned by the choice and colour axes, analogous to **h**. The colour regression vector closely approximates the actual colour input (blue circle) in the motion context, but has a strong component along the choice axis in the colour context. Components along the motion (**h**) and colour (**i**) axes are scaled by a factor of 2 relative to those along the choice axis. **j**, Dot products (colour bar) between the regression vectors (horizontal axis) and the actual model dimensions (vertical axis), computed after setting all norms to 1. The choice regression vector closely approximates the direction of the line attractor in both contexts (squares labelled '1'). As shown also in **h** and **i**, the input regression vectors approximate the model inputs (defined by their synaptic weights) when the corresponding inputs are irrelevant (squares 2 and 4, motion and colour), whereas they approximate the line attractor when relevant (squares 3 and 5). Thus, the motion input is mostly contained in the plane spanned by the choice and motion axes (**h**), and the colour input is mostly contained in the plane spanned by the choice and colour axes (**i**). Finally, the single context regression vector is aligned with both context inputs (squares labelled 6), and closely approximates the difference between the two (not shown).

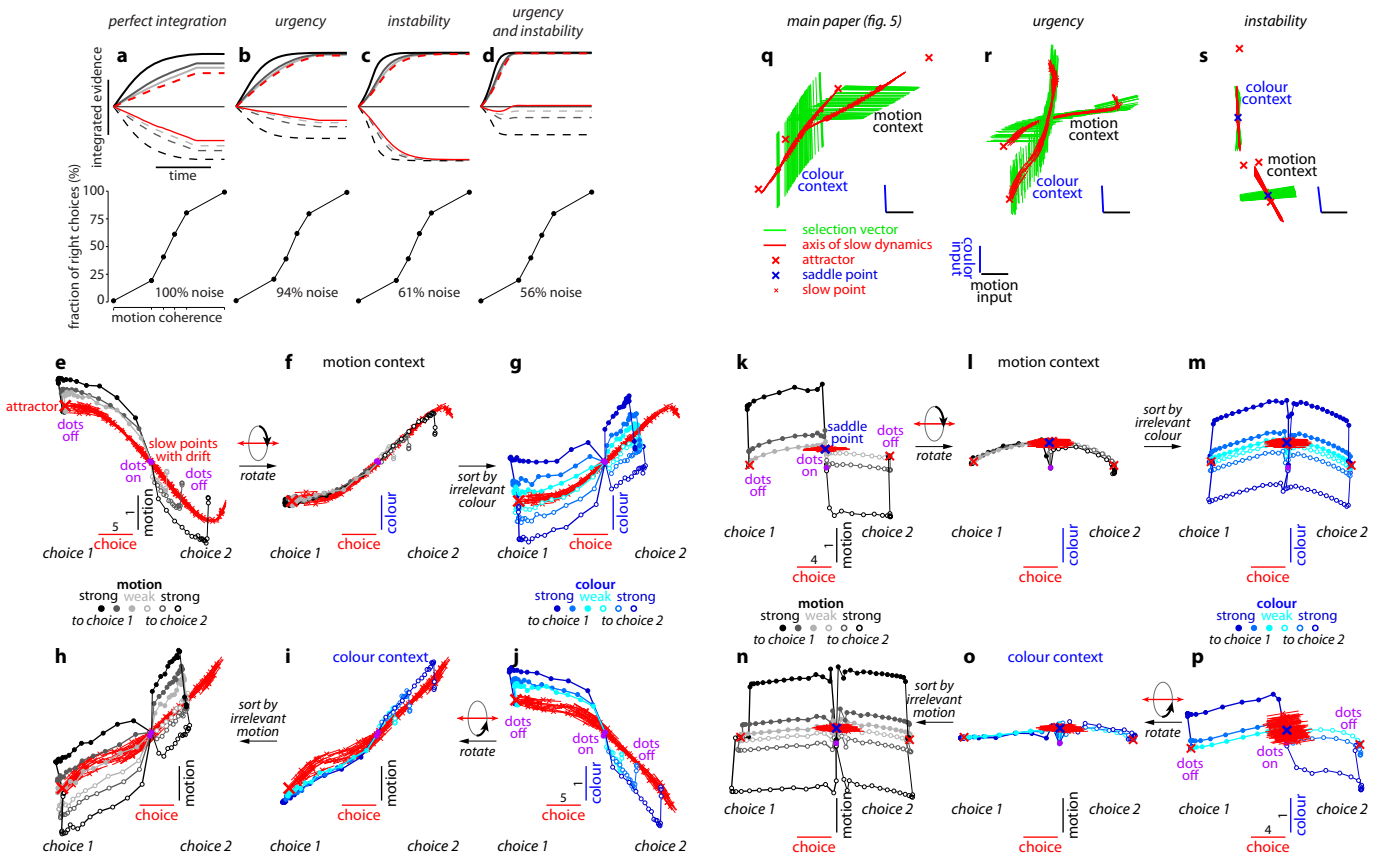

Extended Data Figure 10 | Urgency and instability in the integration process. **a**–**d**, Choice predictive neural activity (top) and psychometric curves (bottom) predicted by several variants of the standard diffusion-to-bound model (see Supplementary Information, section 7.7). **a**, Standard diffusion-to-bound model. Noisy momentary evidence is integrated over time until one of two bounds (+1 or −1; choice 1 or choice 2) is reached. The momentary evidence at each time point is drawn from a Gaussian distribution whose mean corresponds to the coherence of the input, and whose fixed variance is adjusted in each model to achieve the same overall performance (that is, similar psychometric curves, bottom panels). Coherences are 6%, 18% and 50% (the average colour coherences in monkey A, Fig. 1b). Average integrated evidence (neural firing rates, arbitrary units) is shown on choice 1 and choice 2 trials (thick versus thin) for evidence pointing towards choice 1 or choice 2 (solid versus dashed), on correct trials for all coherences (light grey to black, low to high coherence), and incorrect trials for the lowest coherence (red). The integrated evidence is analogous to the projection of the population response onto the choice axis (for example, Extended Data Fig. 5b, top left and bottom right). **b**, Urgency model. Here the choice is determined by a race between two diffusion processes (typically corresponding to two hemispheres), one with bound at +1, the other with bound at −1. The diffusion in each process is subject to a constant drift towards the corresponding bound, in addition to the drift provided by the momentary evidence. The input-independent drift implements an 'urgency' signal, which guarantees that one of the bounds is reached within a short time. Only the integrated evidence from one of the diffusion processes is shown. The three 'choice 1' curves are compressed (in contrast to **a**) because the urgency signal causes the bound to be reached, and integration towards choice 1 to cease, more quickly than in **a**. In contrast, the 'choice 2' curves are not compressed as the diffusion process that accumulates evidence towards choice 1 never approaches a bound on these trials. **c**, Same as **a**, but here the diffusion process is subject to a drift away from the starting point (0) towards the closest bound (+1 or −1). The strength of the drift is proportional to the distance from the starting point, and creates an 'instability' at the starting point. **d**, Same as **b**, with an instability in the integration as in **c** for both diffusion processes. The asymmetry between choice 1 and choice 2 curves in **b** and **d** resembles the asymmetry in the corresponding PFC curves (Extended Data Figs 5b, f, upper left). **e**–**j**, Neural network model with urgency. This model is based on a similar architecture as the model in Fig. 4. Unlike the neural network in Fig. 4, which was trained solely based on the model output on the last time bin of the trial, here the network is trained based on the output it produces throughout the entire input presentation. The network was trained to reproduce the integrated evidence (that is, the decision variable) for one of the two diffusion processes (that is, one of the two 'hemispheres') in a diffusion-to-bound model with urgency (**b**, see Supplementary Information, section 7.7). Similar conventions as in Fig. 5. The urgency signal is controlled by an additional binary input into the network. Here, the urgency and sensory inputs are turned off as soon as a bound is reached. The network generates only a single, stable fixed point in each context, corresponding to the decision boundary (large red cross). The model also implements a series of points of relatively slow dynamics (small red crosses) approximately lying on a single curve. The axes of slow dynamics at these slow points (red lines) are locally aligned. Notably, responses at these slow points have a strong tendency to drift towards the single, stable fixed point (the decision boundary), and thus the curve of slow points does not correspond to an approximate line attractor. This drift implements the urgency signal and causes an asymmetry in the trajectories, which converge on a single point for choice 1, but have endpoints that are parametrically ordered by coherence along the choice axis for choice 2. As discussed below (panel **r**), this model relies on the same mechanism of selection as the original model (Fig. 5, see main text). **k**–**p**, Neural network model with instability. Trajectories show simulated population responses for a model (same architecture as in Fig. 4) that was trained to solve the context-dependent task (Fig. 1) only on high-coherence stimuli and in the absence of internal noise (see Supplementary Information, section 7.7). Same conventions as in Fig. 5. In the absence of noise, prolonged integration of evidence is not necessary for accurate performance on the task. As a consequence, the model implements a saddle point (blue cross) instead of an approximate line attractor. Points of slow dynamics (small red crosses, obscured by the red lines) occur only close to the saddle point. The right zero-eigenvectors of the linearized dynamics around these slow points (red lines) correspond to the directions of slowest dynamics, and determine the direction of the axis of choice. When displaced from the saddle point, the responses quickly drift towards one of the two stable attractors (large red crosses) corresponding to the choices. For a given choice, trajectories for all coherences therefore end in the same location along the choice axis, in contrast to the responses in the original model (Fig. 5). Despite these differences, the original model (Fig. 5) and the network model with instability (**k**–**p**) rely on a common mechanism of context-dependent selection (see panel **s**). **q**–**s**, Dynamical features (key, bottom) underlying input selection and choice in three related neural network models. All models are based on a common architecture (Fig. 4) but are the result of different training procedures. **q**, Dynamical features of the model described in the main paper (Figs 5 and 6), re-plotted from Fig. 6c. **r**, The urgency model (**e**–**j**). **s**, The instability model (**k**–**p**). In all models, the developing choice is implemented as more or less gradual movement along an axis of slow dynamics (specified by the locally computed right eigenvectors associated with the near-zero eigenvalue of the linearized dynamics, red lines). The inputs are selected, that is, result in movement along the axis of slow dynamics, depending on their projection onto the selection vector (the locally computed left eigenvectors associated with the near-zero eigenvalue). In this sense, the three models implement the same mechanisms of context-dependent selection and choice.

doi:10.1038/nature12742

1. Subjects

Two adult male rhesus monkeys, A and F (14 and 12 kg) were trained on a two-alternative, forced-choice, visual discrimination task. Before training, both monkeys were prepared surgically with a head-holding device[1], and monkey A with a scleral search coil for monitoring eye movements[2]. Before electrophysiological recordings, we further implanted a recording cylinder (Crist instruments Co., Inc., Hagerstown, MD) over the arcuate sulcus. Daily access to fluids was controlled during training and experimental periods to promote behavioral motivation. All surgical and behavioral procedures conformed to the guidelines established by the National Institutes of Health and were approved by the Institutional Animal Care and Use Committee of Stanford University.

2. Behavioral task

2.1. Procedures

During both training and experimental sessions monkeys sat in a primate chair with their head restrained. Visual stimuli were presented at 96Hz refresh rate on a CRT monitor placed 43cm from the monkeys' eyes. Eye movements were monitored with a scleral eye coil (*monkey A*, C-N-C Engineering, Seattle, WA) or with an optical eye tracker (*monkeys A and F*, EyeLink 1000, SR Research, ON, Canada); the quality of the latest optical tracker systems are rapidly approaching that of the search coil system[3]. Behavioral control and stimulus presentation were managed by Apple Macintosh G5-based computers (Cupertino, CA) running the Expo software package (Peter Lennie, University of Rochester, NY; Robert Dotson, NYU, NY).

2.2. Task description

On each behavioral trial the monkeys observed a noisy, random-dots motion stimulus presented through a circular aperture. Each random dot stimulus had two properties—motion and color—that the monkey might be required to discriminate, depending upon behavioral context (below). The monkey reported either the prevalent direction of motion or the prevalent color of the stimulus with a saccadic eye movement to one of two visual targets. From trial to trial, motion coherence and color coherence (below) were varied randomly about psychophysical threshold for the discrimination task. Monkeys were rewarded for correct responses with a small quantity of juice.

On any given frame of the stimulus, a fraction of the dots was displayed with one color (color 1), while all others were displayed with a different color (color 2). The difficulty of the color discrimination was varied by parametrically changing the relative number of dots of the two colors, while keeping the total number of dots constant. The fraction of color 1 to color 2 dots, which we call 'color coherence', was fixed throughout the trial (100% coherence: only one color; 0% coherence: equal numbers of dots of the two colors). We define the sign of the color coherence to indicate the dominant color in the stimulus (Fig. 1b, *vertical axis*). In monkey A the dots were either red or green. Monkey F appeared unable to discriminate red and green dots, and was thus trained with blue and orange dots. All colors were matched in luminance.

On each trial a fraction of the dots moved coherently in one of two opposite directions, while the remaining dots were flashed transiently at random locations[4]. The difficulty of the motion discrimination was varied by parametrically changing the fraction of dots moving coherently, which corresponds to the motion coherence of the stimulus (100% coherence: all dots moving in the same direction; 0% coherence: all dots moving randomly). We define the sign of the motion coherence to indicate the direction of coherent motion in the dots (Fig 1b, *horizontal axis*). On any given trial, the motion coherence was identical for dots of color 1 and color 2. Motion and color coherence were chosen randomly on each trial, and were thus completely uncorrelated across trials.

Figure 1a illustrates the sequence of events in each trial. The monkeys initiated a trial by fixating on a small fixation spot, and were subsequently required to maintain fixation within a small window around the fixation point (1.25^{o} radius) until the go cue. The saccade targets appeared 300 ms after the initiation of fixation, and were followed after another 350 ms by the onset of the random-dots. The dots remained on the screen for 750 ms, and their offset was followed by a delay period preceding the go cue. The delay period consisted of an interval of fixed duration (0.3 s) followed by an interval whose duration was drawn from a truncated exponential distribution (mean 0.3 s, truncated at 3 s). The end of the delay period coincided with the disappearance of the fixation point, which served as the go cue, and was followed by the operant saccade to one of the two targets.

The fixation point specified what context the monkey was in. In the motion context, the fixation point was a square, and the monkeys had to discriminate the direction of motion of the dots while ignoring their color. In the color context, the fixation point was a cross, and the monkeys had to discriminate the color of the dots while ignoring their motion. Crucially, both the motion and color evidence were present in the dots on each trial, in one of 36 randomly selected combinations (Fig. 1b).

The two saccade targets varied in location and color from trial to trial (red and green in monkey A, blue and orange in monkey F). In Fig. 1a, for example, the target locations were to the right and left of the dots aperture, and the red and green targets were varied randomly between these two locations from trial to trial. In the motion context, the monkeys were rewarded for saccades to the target location corresponding to the direction of motion of the coherent dots (e.g. a saccade to the right for motion to the right). In the color context, they were rewarded for saccades to the target whose color matched the prevalent color in the dots. We never showed stimuli of 0% motion or color coherence, meaning that each trial could be unambiguously characterized as correct or incorrect. This procedure resulted in half of the trials being 'congruent' (motion and color signals indicating a saccade in the same direction) and half being 'incongruent' (motion and color signals indicating opposite saccades).

The total set of 36 stimuli consisted of all combinations of 6 signed motion coherence levels and 6 signed color coherence levels (Fig. 1b). We varied the coherence levels across monkeys and days to equate performance in the motion and color contexts (average motion coherences: 0.05, 0.15, 0.50 in monkey A, and 0.07, 0.19, 0.54 in monkey F; average color coherences: 0.06, 0.18, 0.50 in monkey A, and 0.12, 0.30, 0.75 in monkey F). For each stimulus the targets could be presented in two configurations (e.g., red target on the right vs. red target on the left) resulting in a total of 72 conditions. These conditions were presented in randomized order within blocks of 72 trials during which the context was kept constant. The end of a block was announced by a tone, and coincided with a change in context. During electrophysiology experiments, the two monkeys completed an average of 28 (monkey A) and 29 blocks per day (monkey F).

3. Electrophysiology experiments

3.1. Procedures

Neurophysiological recordings were performed with tungsten electrodes (2-4MΩ Impedance at 1kHz; FHC Inc., Bowdoin, ME) positioned with a Crist grid (Crist Instruments Co., Inc., Hagerstown, MD) and manipulated with a NAN-drive (NAN Instruments Ltd., Nazareth Illit, Israel). Spiking activity, local field potentials, eye position traces, and digitized task events were recorded using the MAP data-acquisition system (Plexon Inc., Dallas, TX). Spikes were sorted and clustered offline based on principal component analysis using the Plexon offline sorter (Plexon Inc., Dallas, TX). Each well-defined cluster was treated as a 'unit' for the purposes of the analyses. Clusters that did not correspond to well discriminated, single-unit activity were classified as multi-unit activity. All data were analyzed with custom scripts written in MATLAB (The MathWorks, Inc., Natick, MA).

3.2. Recording locations

In both monkeys, the majority of units were recorded in the arcuate sulcus (Extended Data Fig. 1a,f). In monkey A, the recordings also extended rostrally onto the prearcuate gyrus and cortex near and lateral to the principal sulcus. Based on anatomical criteria, a majority of the sulcal recordings most likely targeted the frontal eye fields (FEF). Indeed, in monkey A we evoked saccades with low-current electrical microstimulation at several of the recordings locations lying along the sulcus[5].

We made no systematic attempt to assign the recorded units to FEF or any of the other anatomically or functionally defined areas surrounding FEF[6,7]. All signals we studied—choice, motion, color and context—were distributed throughout the full extent of our recording sites (Extended Data Fig. 1). Moreover, even units whose activity is only weakly task modulated contribute to the signals extracted at the level of the population. We therefore combined the activity of units recorded at all locations into a single population response for each monkey, from which we extract the task related signals described below. For convenience, we refer to the entire area covered by our recordings as 'prefrontal cortex' (PFC).

3.3. Cell selection and task parameters

We typically recorded neural responses simultaneously from two electrodes lowered in adjacent grid holes. The electrodes were advanced until we could isolate at least one single-unit on each electrode. We first characterized the properties of all units with a visually-guided, delayed saccade task, and proceeded with the context-dependent discrimination task if the activity of units on one or both electrodes was modulated during the delay period of the delayed-saccade task. For the discrimination task, one or both saccade targets were placed in the response fields of a subset of the identified units, as characterized with the delayed-saccade task. However, all recorded units were included in the analysis, irrespective of whether they showed delay-period activity during the saccade task, and irrespective of whether one of the targets was in their response field. The random-dot aperture was positioned eccentrically and did not overlap the fixation point or the saccade targets (typical eccentricity: 8-15^{o}, aperture diameter approximately matching the eccentricity). The average eccentricity of the targets was 16^{o} in monkey A and 15^{o} in monkey F.

In monkey A we recorded from 181 single-units and 581 multi-units in 139 penetrations during 80 recording sessions. On average, we recorded 1,280 trials of the context-dependent discrimination task for each unit, for a total of 163,187 behavioral trials. In monkey F we recorded from 207 single-units and 433 multi-units in 108 penetrations during 60 recording sessions. On average, we recorded 1,237 trials for each unit, for a total of 123,550 behavioral trials.

4. Analysis of behavioral data

We constructed average psychometric curves for each monkey by pooling all trials used in the analyses of the electrophysiology data (discussed below). Each trial was assigned a tag based on the strength of the motion evidence (d_1: weak; d_2: intermediate; d_3: strong) and the strength of the color evidence (c_1: weak; c_2: intermediate; c_3: strong). Trials were pooled based on these tags, rather than on the actual coherence values, which changed somewhat across recording sessions. For simplicity in plotting the behavioral data (Fig. 1, Extended Data Fig. 2a-d), we arbitrarily define one of the target locations as being on the right and the other as being on the left, even in sessions where the two targets were only separated along the vertical dimension. Likewise, we define one of the targets as being green and the other one as being red, even though these were not the colors used in monkey F.

The resulting average psychometric curves indicate that both monkeys integrate the motion and color evidence in the random dots differently in the two contexts (Fig. 1, Extended Data Fig. 2a-d). In particular, the motion evidence has a substantially stronger effect on the monkeys' choices during the motion context (Fig. 1c, Extended Data Fig. 2a) than during the color context (Fig. 1e, Extended Data Fig. 2c). Likewise, the color evidence has a substantially stronger effect on choices during the color context (Fig. 1f, Extended Data Fig. 2d) than during the motion context (Fig. 1d, Extended Data Fig. 2b). As a consequence, the monkeys' choices mostly reflect the evidence that is relevant in a given context. The irrelevant evidence is reflected in the choices as well, but weighs less towards the final decision than the relevant evidence (Fig. 1d,e, Extended Data Fig. 2b,c—the slopes are positive).

We fitted the choices of the monkeys with a simple behavioral model based on a previously published model[8] (Fig. 1c-f and Extended Data Fig. 2, curves). In the model, the motion and color inputs are weighted, summed, and then integrated towards a choice. A change in the weights for motion and color inputs across contexts is largely sufficient to account for the different pattern of choices observed in the two contexts.

5. Mathematical notation

The analysis of the electrophysiology data (section 6), as well as the description of the neural network model (section 7), both involve operations on vectors, matrices, and elements thereof. Throughout the Supplementary Information we use the following notation:

(1) *Vectors* are indicated with lower case, bold letters, for example $\boldsymbol{x}$. The k^{th} element of a column vector $\boldsymbol{x}$ is then indicated with the corresponding lower case, non-bold letter, $x(k)$, with k=1 to N for a vector of length N.

(2) *Matrices* are indicated with upper case, bold letters, for example $\boldsymbol{F}$. The element of the matrix $\boldsymbol{F}$ at row k and column j is then indicated with the corresponding upper case, non-bold letter, $F(k,j)$.

(3) *Sets of vectors* are indexed with one or more subscripts, for example $\boldsymbol{x}_i$. The subscript i could for instance index all the units in the population. In that case $\boldsymbol{x}_i$, i=1 to N_{unit}, corresponds to a set of vectors of equal length, one for each unit. Likewise, a set of vectors indexed by unit i and for example time t would be indicated as $\boldsymbol{x}_{i,t}$. The k^{th} element of a given vector in the set is given by $x_{i,t}(k)$.

(4) *Sets of matrices*, in analogy, are also indicated with one or more subscripts, for example $\boldsymbol{F}_{i,t}$. All the matrices in the set have the same number of rows and columns. The element of the matrix $\boldsymbol{F}_{i,t}$ at row k and column j is given by $F_{i,t}(k,j)$.

6. Analysis of electrophysiology data

6.1. Pre-processing

We restrict all our analyses to neural responses occurring during the presentation of the random-dots. For each trial, we computed time-varying firing rates by counting spikes in a 50ms sliding square window (50ms steps). The first window was centered at 100ms after the onset of the random-dots stimulus, the last at 100ms after its offset. This temporal interval starts after a characteristic 'dip' in the responses that appears to precede the integration of evidence in prefrontal and parietal neurons.

6.2. Definition of choice 1 and choice 2

We defined choice 1 as the 'preferred' target for each unit based on the activity during the dots presentation. We grouped trials into two subsets based on the location of the chosen target, and compared responses between the two subsets by computing the area under the ROC curve for the corresponding response distributions[9]. We constructed these distributions by pooling responses across all time samples. We defined the target location eliciting larger responses (in terms of the ROC analysis) as choice 1, and the other target location as choice 2.

6.3. Linear regression

We used multi-variable, linear regression to determine how various task variables affect the responses of each recorded unit. We first z-scored the responses of a given unit by subtracting the mean response from the firing rate at each time and in each trial and by dividing the result by the standard deviation of

the responses. Both the mean and the standard deviation were computed by combining the unit's responses across all trials and times. We then describe the z-scored responses of unit i at time t as a linear combination of several task variables:

$$r_{i,t}(k) = \beta_{i,t}(1)\, choice(k) + \beta_{i,t}(2)\, motion(k) + \beta_{i,t}(3)\, color(k) + \beta_{i,t}(4)\, context(k) + \beta_{i,t}(5), \quad (1)$$

where $r_{i,t}(k)$ is the z-scored response of unit i at time t and on trial k, $choice(k)$ is the monkey's choice on trial k (+1: to choice 1; -1 to choice 2), $motion(k)$ and $color(k)$ are the motion and color coherence of the dots on trial k, and $context(k)$ is the rule the monkey has to use on trial k (+1: motion context; -1: color context). The sign of the motion and color coherence is defined such that positive coherence values correspond to evidence pointing towards choice 1, and negative values to evidence pointing to choice 2. Thus, the sign of color coherence does not just reflect the color of the dots, but also the location of the red and green targets (which on each trial are presented randomly at one of two possible locations). Motion and color coherence are normalized such that values of -1 and +1 correspond to the largest coherence used in a given session.

The regression coefficients $\beta_{i,t}(v)$, for v=1 to 4, describe how much the trial-by-trial firing rate of unit i, at a given time t during the trial, depends on the corresponding task variable v. Here, and below, v indexes the four task variables, i.e. choice (v=1), motion (v=2), color (v=3) and context (v=4). Notably, in addition to these four task variables, the regression model also included all pairwise interaction terms (i.e. products of two task variables). Inclusion of these interaction terms did not have any substantial effects on the main regression coefficients and they are omitted here for clarity. The last regression coefficient (v=5) captures variance that is independent of the four task variables, and instead results from differences in the responses across time. The signal underlying this variance is discussed in more detail below (section 6.10).

To estimate the regression coefficients $\beta_{i,t}(v)$ we first define, for each unit i, a matrix $\boldsymbol{F_i}$ of size $N_{coef} \times N_{trial}$, where N_{coef} is the number of regression coefficients to be estimated (5), and N_{trial} is the number of trials recorded for unit i. The first four rows of $\boldsymbol{F_i}$ each contain the trial-by-trial values of one of the four task variables. The last row consists only of ones, and is needed to estimate $\beta_{i,t}(5)$. The regression coefficients can then be estimated as:

$$\boldsymbol{\beta}_{i,t} = \left(\boldsymbol{F}_i \boldsymbol{F}_i^{\boldsymbol{T}}\right)^{\boldsymbol{-1}} \boldsymbol{F}_i \boldsymbol{r}_{i,t},$$

where $\boldsymbol{\beta}_{i,t}$ is a vector of length N_{coef} with elements $\beta_{i,t}(v)$, v=1-5. Here and below we denote vectors and matrices with bold letters, and use the same letter (not bold) to refer to the corresponding entries of the vector or matrix, which in this case are indexed by v (see Mathematical Notation above).

6.4. Population average responses

We constructed population responses by combining the condition-averaged responses of units that were mostly recorded separately, rather than simultaneously[10,11]. We defined conditions based on the choice of the monkey (choice 1 or choice 2), the signed motion coherence (Fig. 1b, horizontal axis), the signed color coherence (Fig. 1b, vertical axis), context (motion- or color-relevant), and the outcome of

the trial (correct or incorrect). For each unit, trials were first sorted by condition, and then averaged within conditions. We then smoothed the responses in time with a Gaussian kernel (σ = 40ms). Finally, we z-scored the average, smoothed responses of a given unit by subtracting the mean response across times and conditions, and by dividing the result by the corresponding standard deviation. We define the population response for a given condition c and time t as a vector $\boldsymbol{x}_{c,t}$ of length N_{unit} built by pooling the responses across all units for that condition and time. Therefore, the dimension of the state space corresponds to the number of units in the population.

In most figures we analyzed average population responses from correct trials only (note that the linear regression analysis described above was performed on correct *and* incorrect trials). At low coherences, where errors were plentiful, we could plot reliable trajectories for error trials as well (Extended Data Figs. 5 and 9a-e—lowest motion coherence during motion context, lowest color coherence during color context).

In the state-space plots of Fig. 2, we illustrate population responses (trajectories), measured for 36 particularly revealing combinations of these conditions (correct trials only). We first plot trajectories sorted by the relevant sensory signal in each context (Fig. 2a,b and e,f), and then re-plot data from the same trials sorted by the irrelevant sensory signal in each context (Fig. 2c,d):

Figures 2a,b, motion context: 2 choices x 3 relevant motion coherences = 6 trajectories (from 'dots on' to 'dots off'). By definition, when motion is relevant, correct choices occur only when the motion input points *towards* the chosen target (3 conditions per chosen target—strong, intermediate and weak motion towards the chosen target).

Figure 2c, motion context: 2 choices x 6 irrelevant color coherences = 12 trajectories (from 'dots on' to 'dots off'). When color is irrelevant, correct choices can occur for color input pointing *towards* or *away* from the chosen target (6 conditions per chosen target—strong, intermediate and weak color toward *either* target.)

And similarly for the color context:

Figures 2e,f, color context: 2 choices x 3 relevant color coherences = 6 trajectories.

Figure 2d, color context: 2 choices x 6 irrelevant motion coherences = 12 trajectories.

As in the linear regression analysis, trials are not sorted based on the color of the random-dots *per se*, but based on whether the color pointed towards choice 1 or choice 2.

6.5. Targeted dimensionality reduction

To understand the dynamics of PFC activity in our task, it is critical to identify the components of the population responses that are most tightly linked to the monkeys' behavior. Our ultimate goal is to define a small set of axes, within the state space of dimension N_{unit} defined by the activity of each unit, which independently account for response variance due to key task variables (for a related approach see[10,12]). The projection of the population responses onto these axes yields de-mixed estimates of the task-variables, which are mixed at the level of single neurons.

To define the axes of the subspace, we developed a 'Targeted dimensionality reduction' approach, consisting of three steps described in detail below. We start by using principal component analysis (PCA) to de-noise the population responses and focus our analyses on the subspace spanned by the first $N_{pca} = 12$ principal components (PCs). We then identify directions in this reduced subspace (the de-noised regression vectors defined below) that together account for response variance due to four task variables (choice, motion, color, and context). Finally, we orthogonalize the four identified directions to define axes that account for separate components of the variance due to the task variables.

6.6. Principal component analysis

We used PCA to identify the dimensions in state space that captured the most variance in the condition-averaged population responses. We first build a data matrix $\boldsymbol{X}$ of size $N_{unit} \times (N_{condition} \cdot T)$, whose columns correspond to the smoothed, z-scored population response vectors $\boldsymbol{x}_{c,t}$ defined above for a given condition c and time t (section 6.4). $N_{condition}$ corresponds to the total number of conditions, and T to the number of time samples. The PCs of this data matrix are vectors $\boldsymbol{v}_a$ of length N_{unit}, indexed by a from the PC explaining the most variance to the one explaining the least. We use the first N_{pca} PCs to define a de-noising matrix $\boldsymbol{D}$ of size $N_{unit} \times N_{unit}$:

$$\boldsymbol{D} = \sum_{a=1}^{N_{pca}} \boldsymbol{v}_a \boldsymbol{v}_a^T.$$

The de-noised population response for a given condition and time is defined by:

$$\boldsymbol{X}^{pca} = \boldsymbol{D}\,\boldsymbol{X},$$

with $\boldsymbol{X}^{pca}$ also of dimension of size $N_{unit} \times (N_{condition} \cdot T)$. The overall contribution of the a^{th} PC to the population response at each time point t can be quantified by first projecting the population response onto that PC, and then computing the variance across all conditions of the projection, $var(\boldsymbol{v}_a^T \boldsymbol{X})$ (Extended Data Fig. 4b,f).

6.7. Regression subspace

We use the regression coefficients described in Equation 1 above to identify dimensions in state space containing task related variance. For each task variable v=1-4 we first build a set of coefficient vectors $\boldsymbol{\beta}_{v,t}$ whose entries $\beta_{v,t}(i)$ correspond to the regression coefficient for task variable v, time t, and unit i. The vectors $\boldsymbol{\beta}_{v,t}$ (of length N_{unit}) are obtained by simply rearranging the entries of the vectors $\boldsymbol{\beta}_{i,t}$ (of length N_{coef}) computed above (section 6.3). This re-arrangement corresponds to the fundamental conceptual step of viewing the regression coefficients not as properties of individual units, but as the directions in state space along which the underlying task variables are represented at the level of the population. Each vector, $\boldsymbol{\beta}_{v,t}$, thus corresponds to a direction in state space that accounts for variance in the population response at time t, due to variation in task variable v.

We de-noise each vector by projecting it into the subspace spanned by the first $N_{pca} = 12$ principal components:

$$\boldsymbol{\beta}_{v,t}^{pca} = \boldsymbol{D}\,\boldsymbol{\beta}_{v,t},$$

with the set of vectors $\boldsymbol{\beta}_{v,t}^{pca}$ also of length N_{unit}. We refer to these vectors as the 'de-noised' regression coefficients (Extended Data Figs. 1 and 3e,f). This de-noising corresponds to removing from each vector $\boldsymbol{\beta}_{v,t}$ the component lying outside the subspace spanned by the first $N_{pca} = 12$ PCs.

For each task variable v, we then determine the time, t_v^{max}, for which the corresponding set of vectors $\boldsymbol{\beta}_{v,t}^{pca}$ has maximum norm, and define the *time-independent*, de-noised 'regression vectors':

$\boldsymbol{\beta}_v^{max} = \boldsymbol{\beta}_{v,t_v^{max}}^{pca}$ with

$t_v^{max} = \text{argmax}_t \left\| \boldsymbol{\beta}_{v,t}^{pca} \right\|,$

where each $\boldsymbol{\beta}_v^{max}$ is of dimension N_{unit}. Finally, we obtain the orthogonal axes of choice, motion, color, and context (e.g. Fig. 2 and Extended Data Fig. 6) by orthogonalizing the regression vectors $\boldsymbol{\beta}_v^{max}$ with the QR-decomposition:

$\mathbf{B}^{max} = \boldsymbol{Q}\,\boldsymbol{R},$

where $\mathbf{B}^{max} = [\boldsymbol{\beta}_1^{max}\ \boldsymbol{\beta}_2^{max}\ \boldsymbol{\beta}_3^{max}\ \boldsymbol{\beta}_4^{max}]$ is a matrix whose columns correspond to the regression vectors, $\boldsymbol{Q}$ is an orthogonal matrix, and $\boldsymbol{R}$ is an upper triangular matrix. The first four columns of $\boldsymbol{Q}$ correspond to the orthogonalized regression vectors $\boldsymbol{\beta}_v^{\perp}$, which we refer to as the 'task-related axes' of choice, motion, color, and context. These axes span the same 'regression subspace' as the original regression vectors, but crucially each explains distinct portions of the variance in the responses.

To study the representation of the task-related variables in PFC, we projected the average population responses onto these orthogonal axes (Fig. 2 and Extended Data Figs. 4-7):

$$\boldsymbol{p}_{v,c} = \boldsymbol{\beta}_v^{\perp T}\,\boldsymbol{X}_c, \tag{2}$$

where $\boldsymbol{p}_{v,c}$ is the set of time-series vectors over all task variables and conditions, each with length T. Further, we have reorganized the data matrix, $\boldsymbol{X}$, so that separate conditions are in separate matrices, resulting in a set, $\boldsymbol{X}_c$, of $N_{condition}$ matrices of size $N_{unit} \times T$.

The interpretation of the time-series $\boldsymbol{p}_{v,c}$ depends on the exact definition of the associated axes $\boldsymbol{\beta}_v^{\perp}$. In particular, we interpret the projection of the responses onto the choice axis, $\boldsymbol{p}_{1,c}$, as the integrated relevant evidence, and the projection onto the motion axis, $\boldsymbol{p}_{2,c}$, as the momentary motion evidence (Fig. 2). As discussed below (section 7.6), we validated this interpretation on the simulated model responses, for which these quantities can be precisely defined based on the trained network connectivity (Extended Data Fig. 9h-j). Notably, the same interpretation does not hold if the order of the choice and motion regression vectors is inverted in the orthogonalization step, i.e. if the choice axis contained only the component of the choice regression vector that is orthogonal to the motion regression vector. In that case, the choice and motion axes would both represent mixtures of the integrated and momentary evidence, since the motion regression vector effectively lies along a direction that is intermediate between the one representing the integrated evidence and the one representing momentary motion evidence (Extended Data Fig. 9h-j).

Importantly, the geometric relationships between trajectories of different conditions within the regression subspace spanned by either the regression vectors $\boldsymbol{\beta}_v^{max}$, or the orthogonal axes $\boldsymbol{\beta}_v^{\perp}$, are independent of the particular choice of axes used to describe it. For instance, the effects of motion and color on the population response could have occurred along very similar directions in state space (unlike what we found, Fig. 2), even when described with respect to the orthogonal axes of motion and color. In particular, the orthogonality of the vectors in the basis set used to represent the data has no bearing on whether or not any set of trajectories will appear orthogonal in the corresponding subspace.

6.8. Stability of regression subspace

The set of time-series, $\boldsymbol{p}_{v,c}$, are easiest to interpret if a single regression subspace, spanned by the axes $\boldsymbol{\beta}_v^{\perp}$, captures a large fraction of the task-related variance in the population responses at all times and across both contexts. To assess the stability of the regression subspace across both time and contexts we performed the following two analyses.

First, to assess stability of the regression vectors across time, we estimated *time-dependent* axes $\widetilde{\boldsymbol{\beta}}_{v,t}^{\perp}$ of size N_{unit} for the task variables of motion, color, and context, and compared the ability of time-dependent and time-independent axes (section 6.8) to account for variance in the population activity. We obtained the time-dependent axes by orthogonalizing the matrix $\left[\boldsymbol{\beta}_1^{max}\ \boldsymbol{\beta}_{2,t}^{pca}\ \boldsymbol{\beta}_{3,t}^{pca}\ \boldsymbol{\beta}_{4,t}^{pca}\right]$, where the subscript indexes the four task variables. In this analysis, we held the axis of choice constant (as in section 6.7) since a time-dependent choice axis (i.e. using $\boldsymbol{\beta}_{1,t}^{pca}$ instead of $\boldsymbol{\beta}_1^{max}$ in the orthogonalization above) results in a set of four axes that mix representations of the task variables and are thus difficult to relate to the fixed axes $\boldsymbol{\beta}_v^{\perp}$. For instance, early during the dots presentation in the motion context, a time-dependent choice axis would have large projections onto the fixed axes of choice as well as motion, and thus represent a mixture of integrated and momentary motion evidence. This effect occurs because the integrated and momentary relevant evidence are approximately linearly related to each before the 'decision-boundary' is reached, and are thus difficult to de-mix based only on responses collected early during the dots presentation.

At a specific time t, the projections of the population response onto the time-dependent axes are defined by:

$$\widetilde{\boldsymbol{p}}_{v,c}(t) = \widetilde{\boldsymbol{\beta}}_{v,t}^{\perp}{}^{T}\, \boldsymbol{X}_c(:,t),$$

again yielding a time-series of length T for each task variable and condition, but now computed with time-dependent orthogonal axes. At each time point *t,* we then compared the variance across conditions c in $\boldsymbol{p}_{v,c}$ (Extended Data Fig. 4d,h; *solid lines*) to the variance in $\widetilde{\boldsymbol{p}}_{v,c}$ (*dashed lines*). On average across all times, the subspace spanned by the fixed axes of motion, color, and context contains 80% (monkey A) and 78% (monkey F) of the variance captured by the corresponding subspace spanned by time-dependent axes of motion, color, and context. Moreover, the variance has similar time courses along the fixed and time-dependent axes (Extended Data Fig. 4d,h). Overall, these observations imply that the representation of the task variables is largely stable across time.

Second, to quantify the effect of context on the task-related axes, we implemented the steps between equations (1) and (2) twice, separately for responses recorded during the motion and color contexts. This yielded two sets of task-related axes $\boldsymbol{\beta}_v^{mot}$ and $\boldsymbol{\beta}_v^{col}$ (v = 1-3, v =1 is choice axis, v =2 is motion axis and v=3 is the color axis), which describe the representation of choice, motion, and color signals separately in the two contexts. We then projected each context-dependent axis into the fixed regression subspace spanned by $\boldsymbol{\beta}_f^{\perp}$, f= 1-3 and computed its L2-norm:

$$u_v^{mot} = \sqrt{\sum_{g=1}^{3}\left(\boldsymbol{\beta}_v^{mot^T}\,\boldsymbol{\beta}_g^{\perp}\right)^2}$$

$$u_v^{col} = \sqrt{\sum_{g=1}^{3}\left(\boldsymbol{\beta}_v^{col^T}\,\boldsymbol{\beta}_g^{\perp}\right)^2}.$$

The values of u_v^{mot} and u_v^{col} (see Table 1 below) are all close to 1, indicating that the corresponding context-dependent axes lie almost entirely within the regression subspace spanned by the *fixed* axes of choice, motion, and color ($\boldsymbol{\beta}_v^{\perp}$, v = 1-3). Thus a single, fixed set of axes accurately describes the task related responses across both contexts.

	choice	*motion*	*color*
u_v^{mot}	0.98	0.97	0.98
u_v^{col}	0.98	0.98	0.97

Table 1. Overlap between the context dependent axes of choice ($\boldsymbol{v}$ =1), motion ($\boldsymbol{v}$ =2) and color ($\boldsymbol{v}$ =3) and the fixed regression subspace. Numbers correspond to the norm of the projection of a given context-dependent axis into the 3d-subspace spanned by the fixed axes of choice, motion, and color. A norm of 1 implies that a given axis lies entirely within the fixed regression subspace, a norm of 0 that it lies entirely outside.

We also directly compared the direction of the choice axes computed during the motion (u_1^{mot}) and color (u_1^{col}) contexts. These context-dependent choice axes have dot products of 0.92 in monkey A and 0.97 in monkey F, implying that in both monkeys integration of evidence occurs along a direction in state space that is largely stable between contexts.

6.9. Cross validation

We determined to what extent noise in the response of individual units affects the estimation of the regression subspace and the corresponding population trajectories by computing the underlying orthogonal axes $\boldsymbol{\beta}_v^{\perp}$ (Extended Data Fig. 4i-p) and the population trajectories $\boldsymbol{p}_{v,c}$ (Extended Data Fig. 4q,r) twice from non-overlapping subsets of trials. For each unit, we first randomly assigned each trial to one of two subsets, and estimated the corresponding linear regression coefficients separately for the two subsets. These two sets of coefficients were then used to compute two separate sets of axes $\boldsymbol{\beta}_v^{\perp}$ of the regression subspace, following the steps described above. The same two subsets of trials, and the corresponding axes, were then used to generate two sets of population trajectories $\boldsymbol{p}_{v,c}^1$ and $\boldsymbol{p}_{v,c}^2$. To quantify the similarity of trajectories computed from two trial subsets we computed the percentage of variance in the trajectories from one set that is explained by trajectories from the other set (Extended Data Fig. 4q,r, *caption*), for example:

$$100\times\left[1-\sum_{v,c,t}\left(\boldsymbol{p}^1_{v,c}(t)-\boldsymbol{p}^2_{v,c}(t)\right)^2/\sum_{v,c,t}\left(\boldsymbol{p}^1_{v,c}(t)-\langle\boldsymbol{p}^1_{v,c}(t)\rangle_{v,c,t}\right)^2\right],$$

where $\langle\cdot\rangle_{v,c,t}$ indicates the average over all task variables v, conditions c, and time t.

6.10. Urgency signal

The population trajectories in monkey F showed strong evidence for an 'urgency' signal[13,14]—an overall tendency of the population response to move leftward along the choice axis (toward 'choice 1') irrespective of the direction and strength of the sensory input. This signal has the effect of accelerating the usual leftward movement of the population response on trials in which the sensory evidence points toward choice 1 (Extended Data Fig. 7g,l, filled data points) and attenuating or even reversing the usual rightward movement on trials in which the sensory evidence points toward choice 2 (Extended Data Fig. 7g,l, open data points). By definition, units that prefer choice 2 (which we did not record from) would show equivalent effects in the opposite direction.

To compensate for this urgency signal, in monkey F we also computed 'mean-subtracted' population trajectories $\overline{\boldsymbol{p}}_{v,c}$:

$$\overline{\boldsymbol{p}}_{v,c}=\boldsymbol{p}_{v,c}-\langle\boldsymbol{p}_{v,c}\rangle_c,$$

where $\langle\cdot\rangle_c$ indicates the mean over all conditions. The raw time-series, $\boldsymbol{p}_{v,c}$, are shown in Extended Data Figs. 5f-i and 7g-l, the mean subtracted responses in Extended Data Figs. 6c,d and 7a-f.

In the linear regression analysis (section 6.3) any variance due to the passage of time that is common to all conditions is captured by the last regression coefficient in Eq. 1, $\beta_{i,t}(5)$. A regression vector built from these coefficients would lie mostly outside of the subspace spanned by the task-related axes (see also[10]), with the exception of a projection onto the choice axis corresponding to the urgency signal.

7. Neural network model

We trained a fully recurrent neural network (RNN) composed of nonlinear firing-rate units to solve a context-dependent integration task analogous to that performed by the monkeys. The recurrent feedback within the RNN generates rich dynamics that are particularly appropriate for solving dynamical problems such as selection and integration of inputs over time[15]. Our strategy was to train a randomly initialized RNN to solve the task, incorporating minimal assumptions about network architecture. We then reverse-engineered the network using fixed point analysis and linear approximation techniques to identify the mechanistic basis of the solution 'discovered' by the network[16].

7.2. Network equations

We modeled PFC responses with an RNN defined by the following equations:

$$\tau\dot{\boldsymbol{x}}=-\boldsymbol{x}+\boldsymbol{J}\boldsymbol{r}+\boldsymbol{b}^c u_c+\boldsymbol{b}^m u_m+\boldsymbol{b}^{cc}u_{cc}+\boldsymbol{b}^{cm}u_{cm}+\boldsymbol{c}^x+\rho_x \quad (3)$$

$$\boldsymbol{r}=\tanh(\boldsymbol{x})$$

$z = \boldsymbol{w}^T \boldsymbol{r} + c^z$.

The variable $\boldsymbol{x}(t)$ is a 100-dimensional vector containing the 'activation' of each neuron in the network, and $\boldsymbol{r}(t)$ are the corresponding 'firing rates', obtained by the element-wise application of the saturating nonlinearity, $\tanh$, to $\boldsymbol{x}$. Each neuron in the network has a time constant of decay defined by τ=10ms. The matrix $\boldsymbol{J}$ defines the recurrent connections in the network. The network receives 4-dimensional input, $\boldsymbol{u}(t) = [u_c(t)\, u_m(t)\, u_{cc}(t)\, u_{cm}(t)]^T$, through synaptic weights, $\boldsymbol{B} = [\boldsymbol{b}^c\, \boldsymbol{b}^m\, \boldsymbol{b}^{cc}\, \boldsymbol{b}^{cm}]$. These four inputs represent, respectively, the sensory evidence for color and motion, and the contextual cues instructing the network to integrate either the color or the motion input. Finally, the activations contain contributions from a vector of offset currents $\boldsymbol{c}^x$, and from white noise ρ_x drawn at each time step with standard deviation $3.1623 * \sqrt{\Delta t} \approx 0.1$. To read out the network activity, we defined a linear readout (the output neuron in Fig. 4), $z(t)$, as a weighted sum of the firing rates, with weights, $\boldsymbol{w}$, and bias, c^z. During training, the network dynamics were integrated for the duration T of the random-dots (T=750ms) using Euler updates with Δt=1ms. After training, model dynamics were integrated for an additional 200ms during which the sensory inputs were turned off.

7.3. Network inputs and outputs

The motion and color inputs during the context-dependent integration task were each modeled as one-dimensional, white-noise signals:

$u_m(t) = d_m + \rho_m(t)$

$u_c(t) = d_c + \rho_c(t)$.

The white noise terms ρ_m and ρ_c have zero mean and standard deviation $31.623 * \sqrt{\Delta t} \approx 1$ and are added to the offsets d_m and d_c. The sign of the offset on any given trial can be positive or negative, corresponding to evidence pointing towards choice 1 or choice 2, respectively. The absolute values of the offsets correspond to the motion and color coherence. Notably, the color input is not modeled as color *per se*, but directly as color evidence towards choice 1 or choice 2 (as in the definition of the trial-averaged conditions above). During training, the offsets were randomly chosen on each trial from the range [-0.1875 0.1875]. For the simulations (Fig. 5 and Extended Data Figs. 2e-h and 9) we used 3 coherence values (0.009, 0.036, 0.15), corresponding to weak, intermediate, and strong evidence. These values were chosen to qualitatively reproduce the psychometric curves of the monkeys (Extended Data Fig. 2e-h).

To study the local, linearized dynamics of the response, we delivered transient, 1ms duration input pulses of size 2. After delivery of the pulse, the network was allowed to relax with the motion and color inputs set to zero. The pulses resulted in a deflection along the input axes of approximately the same size as the average deflection for the strongest noisy inputs in the context-dependent integration task (Fig. 5).

During both the contextual integration and the pulse experiments, the contextual inputs were constant for the duration of the trial and defined the context. In the motion context $u_{cm}(t) = 1$ and $u_{cc}(t) = 0$, while in the color context $u_{cm}(t) = 0$ and $u_{cc}(t) = 1$, at each time t.

For the purposes of training, we also defined a 'target' signal, $p(t)$, corresponding to the desired output of the network. The target was defined at only two time steps in each trial. At the first time step (i.e. the onset of the random-dots) the target was zero, i.e. $p(\Delta t) = 0$. At the last time step T (i.e. the offset of the random-dots) the target was either +1 or -1, and corresponded to the correct choice given the inputs and the context. In particular, the sign of the target at time T corresponded to the sign of the motion offset d_m in the motion context, and the sign of the color offset d_c in the color context. At all other time steps between Δt and T the target was undefined, meaning the output value of the network was completely unconstrained and had no impact on synaptic modification.

7.4. Network training

Before training, the network was initialized using standard random initialization. Specifically, the matrix elements J_{ik} were initialized from a normal distribution with zero mean and variance $1/N$, where N=100 is the number of neurons the network. The inputs $\boldsymbol{B}$ were initialized from a normal distribution with zero mean and standard deviation 0.5. The output weights $\boldsymbol{w}$ were initialized to zero. We generated $S = 160{,}000$ trials with randomized inputs to train the network.

We used Hessian-Free optimization for training recurrent neural networks[17,18] (RNNs), which utilizes back-propagation through time[19] (BPTT) to compute the gradient of the error with respect to the synaptic weights. The error was defined as:

$$\frac{1}{ST}\sum_{s\in[1..S]}\sum_{t=\Delta t,T}\left(z_s(t)-p_s(t)\right)^2,$$

where the first sum is over all S trials, and the second over the first and last time steps of the trial. The Hessian-Free method is a second-order optimization method that computes Newton steps. It was recently shown to help ameliorate the well-known vanishing gradient problem[20] associated with training RNNs using BPTT. The input to this supervised training procedure was the initialized RNN, and the input-target pairs that define the context-dependent integration. The result of the training procedure was the set of modified synaptic weights, $\boldsymbol{J}$, $\boldsymbol{B}$, and $\boldsymbol{w}$, the offset currents $\boldsymbol{c}^x$, and the bias, c^z.

The two context-dependent initial conditions of the network at the onset of the trial were not optimized as above. Nevertheless, to prevent small transient activations at the beginning of each trial, we defined the initial conditions with the following procedure. First, we trained two stable fixed points, one for each context. For this purpose, we set $u_c(t)$ and $u_m(t)$ to zero, and either $u_{cc}(t) = 1$ and $u_{cm}(t) = 0$ (motion context) or $u_{cc}(t) = 0$ and $u_{cm}(t) = 1$ (color context). During the first half of the training of the context-dependent integration we used these fixed points as initial conditions. Halfway through the training, and again at the end of training, we found the context-dependent slow points of the dynamics (see below) and reset each initial condition to the slow point resulting in the output closest to zero. Critically, responses beyond the first few time steps after stimulus onset, as well as the dynamical structure uncovered by the fixed-point analysis (see below), did not depend on the choice of initial conditions.

7.5. Fixed point analysis

To discover the dynamical structure of the trained RNN, we followed procedures established by Sussillo and Barak[16]. We found a large sample of the RNN's fixed points and slow points by minimizing the function:

$$q(x) = \frac{1}{2}|\boldsymbol{F}(\boldsymbol{x})|^2,$$

where $\boldsymbol{F}(\boldsymbol{x})$ is the RNN update equation (i.e. the right-hand side of Eq. 3). The function $q(\boldsymbol{x})$ loosely corresponds to the squared speed of the system. Since the network effectively implements two dynamical systems, one for each context, we studied the dynamics separately for the motion and color contexts (see the sine wave generator example in[16]). In each context, we first found the two stable fixed points at the end of the approximate line attractor by setting a tolerance for $q(\boldsymbol{x})$ to 1e-25. To find slow points on the line attractor, we ran the $q(\boldsymbol{x})$ optimization 75 times with a tolerance of 1.0. The identified slow points are approximate fixed points with a very slow drift, which is negligible on the time scale of the normal network operation. These slow points are referred to as fixed points throughout the main text. Any runs of the optimization that found points with $q(\boldsymbol{x})$ greater than the predefined tolerance were discarded and the optimization was run again.

We performed a linear stability analysis around each of the identified slow points, $\boldsymbol{x}^*$. We used the first order Taylor series approximation of the network update equation (Eq. 3) around $\boldsymbol{x}^*$ to create a linear dynamical system, $\dot{\delta\boldsymbol{x}} = \boldsymbol{F}'(\boldsymbol{x}^*)\delta\boldsymbol{x}$, and then performed an eigenvector decomposition on the matrix $\boldsymbol{F}'(\boldsymbol{x}^*)$ to obtain a set of left and right eigenvectors, $\boldsymbol{L}$ and $\boldsymbol{R}$ (see section 10 below). For all linear systems one eigenvalue was approximately zero, while all other eigenvalues had a substantially negative real part. The right and left eigenvectors associated with the zero eigenvalue correspond to the line attractor and the selection vector, respectively.

A short introduction to the theory of linear dynamical systems, as well as a detailed description of the procedures underlying the fixed-point analysis of RNNs, are provided in the first half of section 10. The specific mechanism underlying context-dependent selection and integration in the trained RNN is discussed in the second half of section 10.

7.6. Network population responses

We constructed population responses for the RNN following the same procedures as for the PFC data. To display trajectories in state space (e.g. Fig. 5), we projected the population responses onto the axes of a subspace that is analogous to the regression subspace estimated from the PFC data (Extended Data Fig. 9h-j). We found the 'model axes' by orthogonalizing the direction of the right zero eigenvectors averaged over slow points and contexts, and the input vectors, $\boldsymbol{b}^c$ and $\boldsymbol{b}^m$. These model axes closely match the axes of choice, motion, and color estimated with linear regression on the simulated model responses (Extended Data Fig. 9h-j). Unlike the estimated axes, however, the model axes can be defined exactly from the weight matrix of the network, and ultimately directly control the dynamics in the model. The population responses are built from the activations, $\boldsymbol{x}$, because they are directly related to the linear dynamics around the fixed points (see below). Population responses built from the activations are qualitatively similar to population responses built from the firing rates $\boldsymbol{r}$.

7.7. Urgency and instability models

The dynamics of responses along the choice axis in PFC differ somewhat from those observed in our neural network model. In particular, the slopes of the choice predictive signals in PFC depend less on the relevant stimulus coherence than in the model. Moreover, the effects of relevant coherence are asymmetric for the two choices in PFC, but not in the model (compare Extended Data Figs. 5b,f and 9b, *top-left* and *bottom-right*). These differences between the model and the physiological dynamics can be readily explained by previously proposed imperfections in the evidence integration process, such as 'urgency' signals[13,14] or instability in the integrator[21] (Extended Data Fig. 10).

We first studied the effects of urgency and instability on choice predictive activity by modifying a diffusion-to-bound model[22,23]. The temporal evolution of the decision variable $d(t)$ (i.e. of the integrated evidence) is modeled as:

$$d(t + \Delta t) = d(t) + \Delta t \cdot v(t)$$

where $v(t)$ is the drift rate of the diffusion process at time t. The drift rate is given by:

$$v(t) = k\big(C + \kappa + \rho_d(t)\big) + \mu + \lambda d(t)$$

where C is the coherence of the relevant input, $\mu > 0$ is the urgency signal, $\lambda d(t)$ is a drift away from the starting point ($x = 0$) that makes the integration process unstable ($\lambda > 0$), $\rho_d(t)$ is within-trial noise drawn from a normal distribution with standard deviation $\sigma/\sqrt{\Delta t}$, and κ is across-trial noise drawn from a normal distribution with standard deviation ϑ. The diffusion process ends when the decision variable reaches the bound A, i.e. when $d(t) \geq A$, $A > 0$. Here we assume that the choice is the result of a race between two such diffusion processes, one that integrates evidence in favor of choice 1, and the other in favor of choice 2. The diffusion process that first reaches the bound wins the race and determines the choice. The two processes differ only in the parameter k; for the first diffusion process $k = +\alpha$, and for the second $k = -\alpha$, $\alpha > 0$. Even though we used both processes to simulate the behavior, we then computed the integrated evidence in Extended Data Fig. 10a-d by averaging the decision variable from only one of the two processes. The four models in Extended Data Fig. 10a-d are based on the following parameters:

	α	σ	ϑ	μ	λ	A
standard	0.3	0.18	0	0	0	0.05
urgency	0.3	0.17	0	0.04	0	0.05
instability	0.3	0.11	0	0	8	0.05
urgency & instability	0.3	0.10	0	0.04	8	0.05

Table 2. Diffusion model parameters.

We built neural network models that implement instability in the integration or an urgency signal using two different approaches. To build a model with instability (Extended Data Fig. 10k-p and 10s) we used the same approach as in the original model (Fig. 4 and 5), with one important exception: during training of the network we "turned off" the noise in the motion and color inputs ($\rho_m = 0$ and $\rho_c = 0$, section 7.3) as well as the noise in the internal activations of the hidden units of the RNN ($\rho_x = 0$, section 7.2).

To build a model with urgency (Extended Data Fig. 10e-j and 10r) we instead directly trained a neural network model to reproduce the output of a diffusion model with urgency. More precisely, we defined the target signal (section 7.3) as $p(t) = d(t)/A$, where $d(t)$ is the decision variable for one of the two diffusion processes, and A is the decision boundary. We simulated the diffusion model with the following parameters: $\alpha = 0.3, \sigma = 0.1, \vartheta = 0.25, \mu = 0.035, \lambda = 0, A = 0.05$. For all times between the time of the choice (i.e. the time of boundary crossing in one of the diffusion processes) and the end of the stimulus presentation ($t = 750ms$) $x(t)$ was set to its value on the last time step before the choice. The network architecture was analogous to that of the original model (Fig. 4) with the exception of an additional urgency input of constant value 1. On each trial, the relevant sensory input to the RNN (u_m during motion context, u_c during color context, section 7.3) corresponded to the input used to simulate the diffusion process ($C + \kappa + \rho_d(t)$), scaled to have a within-trial standard deviation of $3.1623 * \sqrt{\Delta t} \approx 0.1$. The irrelevant sensory input was generated in an analogous fashion, but had no bearing on $d(t)$. In this model both the motion and color inputs, as well as the urgency input, were turned off after the time of the choice. For the simulations in Extended Data Fig. 10e-j we used three coherence values C (0.12, 0.25. 0.50) that were higher than in the original model (Fig. 5). These coherence values and diffusion model parameters were chosen to achieve a qualitative match between the model predictions and the data for monkey A (both behavior and population trajectories). Different parameters or coherences result in network models with dynamical features analogous to those in Extended Data Fig. 10r.

8. Simulation of alternative population responses

To demonstrate that the properties of the population responses observed in PFC are not a trivial consequence of our analysis methods, we simulated population responses expected from the four basic mechanisms of context-dependent selection illustrated in the cartoon drawings in Fig. 3 of the main text (Extended Data Fig. 8). These simulations are based on the assumption that the responses of individual PFC neurons represent mixtures of the following four task variables: (1) the momentary motion evidence, $s^m(t)$; (2) the momentary color evidence, $s^c(t)$; (3) the integrated relevant evidence, $s^r(t)$ (integrated motion evidence in the motion context, integrated color evidence in the color context); (4) context, $s^x(t)$. Our strategy was to construct four variants of a diffusion-to-bound model of decision-making, each mimicking one of the selection mechanisms in Fig. 3 of the main text. As described below, each variant was constructed by altering the weightings of the four task variables (listed above) onto simulated single units. Each of the underlying selection mechanisms features highly heterogeneous, mixed coding like that commonly observed in PFC, yet each is characterized by a distinct, readily identifiable pattern of population activity in state space. In addition, we show that standard "single unit" regression analyses of the simulated data are singularly unhelpful in revealing the underlying mechanisms, and in one common analysis, generate conclusions that are simply wrong.

8.1. Mixtures of task variables

We simulated each task variable, $s^m(t), s^c(t), s^r(t)$ and $s^x(t)$ for 500 experimental sessions of 1296 trials each (see section 8.2 below); for example, $s^r_{i,k}(t)$ is the integrated relevant evidence for session i on trial k at time t. We then simulated the responses of *sequentially* recorded neurons (one per

session), by mixing the task variables from a given experimental session. Specifically, we generated the firing rate responses of neuron i by mixing the task variables for session i:

$$r_{i,k}(t) = \alpha_m(i)s^m_{i,k}(t) + \alpha_c(i)s^c_{i,k}(t) + \alpha_r(i)s^r_{i,k}(t) + \alpha_x(i)s^x_{i,k}(t) + r_b + noise,$$

where the mixing weights correspond to the components of four "mixing vectors" $\boldsymbol{\alpha}_m$, $\boldsymbol{\alpha}_c$, $\boldsymbol{\alpha}_r$, and $\boldsymbol{\alpha}_x$, r_b is the baseline response, and the $noise$ is drawn from a normal distribution of zero mean. The standard deviation of the $noise$ was chosen such that the variability in $r_{i,k}(t)$ is consistent with a point process with Fano factor of 1.

We simulated population responses corresponding to different selection mechanisms by varying the relationship between the four mixing vectors. We first built four nearly orthogonal 500-dimensional vectors $\boldsymbol{\alpha}_1$, $\boldsymbol{\alpha}_2$, $\boldsymbol{\alpha}_3$, and $\boldsymbol{\alpha}_4$ whose components were randomly drawn from a normal distribution. We then defined the mixing vectors as follows:

Observed PFC responses (Extended Data Fig. 8a-c and Fig. 3a). To simulate population responses resembling those we observed in PFC, we set $\boldsymbol{\alpha}_r = \boldsymbol{\alpha}_1$, $\boldsymbol{\alpha}_m = \boldsymbol{\alpha}_2$, $\boldsymbol{\alpha}_c = \boldsymbol{\alpha}_3$, and $\boldsymbol{\alpha}_x = \boldsymbol{\alpha}_4$ on all trials. Thus "mixed selectivity" is a standard feature of the simulated unit responses; all signals contribute to the responses of individual "units", with weights being randomly mixed across units.

Context-dependent early selection (Extended Data Fig. 8d-f and Fig. 3b). To simulate population responses expected by context-dependent early selection, we set $\boldsymbol{\alpha}_r = \boldsymbol{\alpha}_1$ and $\boldsymbol{\alpha}_x = \boldsymbol{\alpha}_4$ on all trials, $\boldsymbol{\alpha}_m = \boldsymbol{\alpha}_1$, $\boldsymbol{\alpha}_c = 0.2\,\boldsymbol{\alpha}_1$ in the motion context, and $\boldsymbol{\alpha}_m = 0.2\,\boldsymbol{\alpha}_1$, $\boldsymbol{\alpha}_c = \boldsymbol{\alpha}_1$ in the color context. Again, all signals contribute to the responses of individual units, although the weights of the irrelevant momentary evidence are on average 5 times smaller than those of the relevant momentary evidence (corresponding to the ratio between the corresponding behavioral weights, h_m and h_c, see below).

Context-dependent input direction (Extended Data Fig. 8g-i and Fig. 3c). To simulate population responses expected by context-dependent input directions, we set $\boldsymbol{\alpha}_r = \boldsymbol{\alpha}_1$ and $\boldsymbol{\alpha}_x = \boldsymbol{\alpha}_4$ on all trials, $\boldsymbol{\alpha}_m = \boldsymbol{\alpha}_1$, $\boldsymbol{\alpha}_c = \boldsymbol{\alpha}_3$ in the motion context, and $\boldsymbol{\alpha}_m = \boldsymbol{\alpha}_2$, $\boldsymbol{\alpha}_c = \boldsymbol{\alpha}_1$ in the color context. As above, all signals contribute to the responses of individual units, but the ensemble representation of the sensory inputs (i.e. the state space direction) varies across contexts.

Context-dependent output direction (Extended data Fig. 8j-l and Fig. 3d). To simulate population responses expected by context-dependent output direction, we set $\boldsymbol{\alpha}_m = \boldsymbol{\alpha}_2$, $\boldsymbol{\alpha}_c = \boldsymbol{\alpha}_3$, $\boldsymbol{\alpha}_x = \boldsymbol{\alpha}_4$ on all trials, $\boldsymbol{\alpha}_r = \boldsymbol{\alpha}_2$ in the motion context, and $\boldsymbol{\alpha}_r = \boldsymbol{\alpha}_3$ in the color context. Yet again, mixed selectivity is typical of unit responses, but the ensemble representation of the choice varies across contexts.

Importantly, the same four task variables are mixed in the neural population in all four cases—the four simulations differ only in the geometrical relationship between the corresponding mixing vectors, not in the strength of the corresponding task variables (with the exception of *early selection*, where the irrelevant momentary evidence is strongly attenuated with respect to the relevant momentary evidence).

We then analyzed these simulated population responses by applying the same methods used to analyze the responses recorded in PFC (Extended Data Fig. 8; Supp. Information, sections 6.3-6.8). Traditional single unit regression methods reveal a multitude of signals that are mixed at the level of single neurons,

as expected, but provide little obvious insight into how these signals are represented in the population (compare Extended Data Fig. 8b,e,h,k). In fact, the raw regression coefficients obtained with linear regression ($\boldsymbol{\beta}_{v,t_v^{max}}$ in section 6.7) can be rather misleading. The regression coefficients of choice, for example, are correlated with the coefficients of motion (Extended Data Fig. 8b, *top left*) and color (*top middle*), even when by construction the inputs and the integrated evidence are represented along orthogonal directions in state space (i.e. $\boldsymbol{\alpha}_r$, $\boldsymbol{\alpha}_m$, and $\boldsymbol{\alpha}_c$). Moreover, estimating the overall strength of the motion and color inputs in the population by simply averaging the absolute values of the corresponding regression coefficients leads to the erroneous conclusion that the relevant input is stronger than the irrelevant input (e.g. Extended Data Fig. 8c,i,l), even when by construction the inputs are not modulated by context. The trajectories computed with targeted dimensionality reduction, on the other hand, faithfully capture the properties of the task variables as specified by the mixing vectors and clearly distinguish between the different selection mechanisms (compare Extended Data Fig. 8a,d,g,j).

Importantly, the data in Extended Data Fig. 8, unlike the cartoons in Fig. 3, reflect actual simulations of population responses based on the diffusion-to-bound model. We generated population responses expected from the four selection mechanisms by imposing different relationships between the mixing vectors. Despite the very different underlying mixing vectors, the resulting population responses are generically similar in that they all incorporate, 1) mixed selectivity at the single unit level, and 2) coding of irrelevant as well as relevant sensory information in the population (with the exception of early selection, where the irrelevant input is attenuated; see above). Critically, when analyzed with our targeted dimensionality reduction technique, each mechanism gives rise to a distinct pattern of state space trajectories that matches nicely to the corresponding cartoon pattern in Fig. 3 of the main text (compare the left column of Extended Data Fig. 8a,d,g,j, gray scale traces, to text Fig. 3a,b,c,d). Thus the structure of the observed PFC population responses (e.g. Fig. 2) is not "imposed" by our analysis methods, and is not an inevitable consequence of the existence of mixed signals in single units.

8.2. Generation of task variables

We generated the four task variables by simulating a diffusion model (see also section 7.7). The integrated evidence is based on the time-dependent decision variable, $s^r(t) = d(t)$, where:

$$d(t + \Delta t) = d(t) + \Delta t \cdot v(t).$$

The underlying drift of the diffusion process $v(t)$ here is computed as:

$$v(t) = h_m s^m(t) + h_c s^c(t) + \mu,$$

where $s^m(t)$ and $s^c(t)$ are the momentary motion and color evidence, respectively, and $\mu = 0.1$ is the urgency signal. The diffusion process ends when the decision variable reaches the bound $A = 0.1$. The motion gain h_m is 0.8 during the motion context, and 0.16 during the color context. Likewise, the color gain h_c is 0.16 during the motion context, and 0.8 during the color context. The momentary motion and color evidence are defined as:

$$s^m(t) = C_m + \kappa_m + \rho_m(t)$$

and

$s^c(t) = C_c + \kappa_c + \rho_c(t)$.

The within-trial noise $\rho_m(t)$ and $\rho_c(t)$ is drawn from normal distributions with standard deviation $\sigma/\sqrt{\Delta t}$, $\sigma = 0.05$, and the across-trials noise κ_m and κ_c is drawn from normal distributions with standard deviation $\vartheta = 0.25$. Finally, the context signal is a constant, $s^x(t) = 1$ in the motion context, and $s^x(t) = -1$ in the color context. We simulated the diffusion process for all combinations of 6 motion coherences C_m (±0.03, ±0.12, ±0.5), 6 color coherences C_c (±0.03, ±0.12, ±0.5), and two contexts (motion and color context), for a total of 6x6x2=72 conditions. We simulated each condition 18 times within each experimental session, for a total of 1296 trials per session.

The diffusion model variables $s^m(t)$, $s^c(t)$, $s^r(t)$ and $s^x(t)$ for session i and trial k are then scaled to obtain the task variables $s^m_{i,k}(t)$, $s^c_{i,k}(t)$, $s^r_{i,k}(t)$ and $s^x_{i,k}(t)$ (see section 8.1 above), which are mixed to obtain the simulated neural firing rates. The task variables are defined as: $s^m_{i,k}(t) = 0.04 \cdot s^m(t)$, $s^c_{i,k}(t) = 0.04 \cdot s^c(t)$, $s^r_{i,k}(t) = 1 \cdot s^r(t)$, $s^x_{i,k}(t) = 0.02 \cdot s^x(t)$. These scaling factors are fixed across the four selection mechanisms, and result in simulated population responses (Extended Data Fig. 8a-c) with across-condition variance along the task related axes of choice, motion, color, and context that qualitatively match those observed in PFC (e.g. Fig. 2 and Extended Data Fig. 6).

9. Supplementary references

1 Evarts, E. V. A technique for recording activity of subcortical neurons in moving animals. *Electroencephalogr Clin Neurophysiol* **24**, 83-86, (1968).

2 Judge, S. J., Richmond, B. J. & Chu, F. C. Implantation of magnetic search coils for measurement of eye position: an improved method. *Vision Res* **20**, 535-538, (1980).

3 Kimmel, D. L., Mammo, D. & Newsome, W. T. Tracking the eye non-invasively: simultaneous comparison of the scleral search coil and optical tracking techniques in the macaque monkey. *Front Behav Neurosci* **6**, 49, (2012).

4 Britten, K. H., Shadlen, M. N., Newsome, W. T. & Movshon, J. A. The analysis of visual motion: a comparison of neuronal and psychophysical performance. *J Neurosci* **12**, 4745-4765, (1992).

5 Bruce, C. J., Goldberg, M. E., Bushnell, M. C. & Stanton, G. B. Primate frontal eye fields. II. Physiological and anatomical correlates of electrically evoked eye movements. *J Neurophysiol* **54**, 714-734, (1985).

6 Petrides, M. Lateral prefrontal cortex: architectonic and functional organization. *Philos Trans R Soc Lond B Biol Sci* **360**, 781-795, (2005).

7 Schall, J. D. in *Cerebral Cortex* Vol. 12 (eds K.S. Rockland, J. H. Kaas, & A. Peters) (Plenum Press, 1997).

8 Gold, J. I. & Shadlen, M. N. The influence of behavioral context on the representation of a perceptual decision in developing oculomotor commands. *J Neurosci* **23**, 632-651, (2003).

9 Shadlen, M. N. & Newsome, W. T. Neural basis of a perceptual decision in the parietal cortex (area LIP) of the rhesus monkey. *J Neurophysiol* **86**, 1916-1936, (2001).

10 Machens, C. K., Romo, R. & Brody, C. D. Functional, but not anatomical, separation of "what" and "when" in prefrontal cortex. *J Neurosci* **30**, 350-360, (2010).

11 Churchland, M. M. *et al.* Neural population dynamics during reaching. *Nature* **487**, 51-56, (2012).

12 Machens, C. K. Demixing population activity in higher cortical areas. *Front Comput Neurosci* **4**, 126, (2010).

13 Churchland, A. K., Kiani, R. & Shadlen, M. N. Decision-making with multiple alternatives. *Nat Neurosci* **11**, 693-702, (2008).

14 Reddi, B. A. & Carpenter, R. H. The influence of urgency on decision time. *Nat Neurosci* **3**, 827-830, (2000).

15 Sussillo, D. & Abbott, L. F. Generating coherent patterns of activity from chaotic neural networks. *Neuron* **63**, 544-557, (2009).

16 Sussillo, D. & Barak, O. Opening the black box: low-dimensional dynamics in high-dimensional recurrent neural networks. *Neural Comput* **25**, 626-649, (2013).

17 Martens, J. & Sutskever, I. Learning recurrent neural networks with hessian-free optimization. *Proceedings of the 28th International Conference on Machine Learning.* (2011).

18 Martens, J. Deep learning via Hessian-free optimization. *Proceedings of the 27th International Conference on Machine Learning.* (2010).

19 Werbos, P. J. Backpropagation through time: what it does and how to do it. *Proceedings of the IEEE.* 1550-1560 (1990).

20 Bengio, Y., Simard, P. & Frasconi, P. Learning long-term dependencies with gradient descent is difficult. *IEEE Transactions on Neural Networks.* 157-166 (1994).

21 Brunton, B. W., Botvinick, M. M. & Brody, C. D. Rats and humans can optimally accumulate evidence for decision-making. *Science* **340**, 95-98, (2013).

22 Smith, P. L. & Ratcliff, R. Psychology and neurobiology of simple decisions. *Trends Neurosci* **27**, 161-168, (2004).

23 Palmer, J., Huk, A. C. & Shadlen, M. N. The effect of stimulus strength on the speed and accuracy of a perceptual decision. *J Vis* **5**, 376-404, (2005).

10. Mathematical explanation of selective integration in the RNN

Introduction

The standard equations to define an RNN are given by

$$\tau \dot{x}_i = -x_i + \sum_k^N J_{ik} r_k + \sum_k^I B_{ik} u_k + b_i^x \tag{1}$$

$$r_i = \mathrm{h}(x_i) \tag{2}$$

$$z = \sum_k^N w_k r_k + b^z, \tag{3}$$

where x_i is the "activation" of the i^{th} neuron, and $r_i = \mathrm{h}(x_i)$ is the associated "firing rate", defined as the application of the saturating nonlinear function. Each of the N neurons in the network has a time constant of decay defined by τ, and so in isolation an individual neuron acts as a low-pass filter. The recurrence of the network is defined by the matrix $\mathbf{J}$ and it is this feedback that gives the RNN its power, along with the nonlinearity on the firing rates. The matrix elements, J_{ik}, are initialized from a normal distribution with zero mean and variance, $1/N$. The network receives I-dimensional input, $\mathbf{u}(t)$, through synaptic weights $\mathbf{B}$. Finally, there is a vector of offset currents, $\mathbf{b}^x$. In order to read out the network solution to a given problem, it is common to define a linear readout, z, defined as a weighted sum of the firing rates with weights $\mathbf{w}$, plus a bias, b^z.

These networks are not spiking networks. One typically thinks of a single firing rate variable, r_i, as being the population averaged firing rate of many spiking neurons[1]. In an RNN, the activation and firing rate variables, x_i and r_i, can take analog values, again like a population average of spiking neurons. Further, the network is continuous in time. The natural time scales of the network are related to both τ and the nature of the feedback as defined by $\mathbf{J}$.

The selective integrating RNN (siRNN) employed in this paper parametrizes equation 1 with $N = 100$, $I = 4$ (the two sensory inputs of color and motion as well as the two contextual inputs for color and motion, $\mathbf{B} = [\mathbf{b}^c\ \mathbf{b}^m\ \mathbf{b}^{cc}\ \mathbf{b}^{cm}]$), $\tau = 10$ms and h() = tanh(). The values of the weights and biases were set via an optimization approach described in the Suppl. Information section 7.4.

Motivation of our approach

Most often in computational studies in neuroscience a network model is designed by hand to implement a specific function, such as a decision[2], or auto completion of memories[3].

This study was different. Instead we took a machine learning approach and trained the RNN with a powerful optimization technique, specifically the Hessian-Free optimization technique recently proposed for neural networks by Martens and Sutskever[4]. We make no claims about the biological validity of the training approach. Rather, our goal was to study solutions to the problem of selective integration that were nonlinear, dynamical and distributed (i.e. implemented by the interactions of simple units), and where the solution was not explicitly built into the network. We trained many networks (around 100) from different initializations of the weights and biases, and each time the network solved the problem in the same qualitative way. This points to the fact that the selective integration task (see Fig. 1 in main text) placed strong constraints on the optimization process.

The Hessian-Free optimization technique is a supervised learning algorithm, which means that the training routine compares the actual outputs of the RNN to the desired outputs and changes the synaptic weights and biases to reduce this error. Because the supervised training algorithm specifies *which* function to perform without specifying *how* to perform it, the precise mechanisms underlying an RNN's solution are often completely opaque. Such a network is often referred to as a "black box", implying that it fundamentally cannot be understood. However, new techniques have recently been developed for understanding RNN functionality[5], and we employ these approaches extensively in the current paper. Our aim was to "crack" open the network and potentially discover novel solutions to the problem of selective integration.

In what follows, we explain how the trained siRNN functions. We proceed in a general analytic sequence: defining fixed points and line attractors, linearization around fixed points, and using the eigenvector decomposition to understand dynamics of linear systems. This very general approach to elucidating network mechanism is mandated by our original decision to train the siRNN without building in any specific solution to the computational problem. Achieving a post hoc understanding of the trained siRNN, or indeed any system trained in this manner, is greatly facilitated by this sequence of analyses, which are described individually in the next several sections. Readers who are already familiar with these techniques may wish to skip ahead to the section entitled, "Understanding selective integration", which provides a concise explanation of how the siRNN works. We omit precise details of the siRNN training procedure, which are provided in Suppl. Information section 7.4.

Understanding how the network functions

Fixed points and line attractors

As shown in the main article, the siRNN creates two approximate line attractors, each bounded at both ends by a stable attractor. The line attractors are defined by the context

input, meaning only one line attractor ever exists during a given trial. Depending on the contextual input (i.e. the motion context or the color context), a line attractor implements an accumulation of noisy evidence of one or the other input streams. Once the RNN has accumulated enough evidence, and in so doing, moved along the line far enough in either direction, the network dynamics become fixed in one of two attractor states at either end of the line attractor, representing the decision made by the RNN.

Surprisingly, given the relative simplicity of the system, to good approximation we can understand the behavior of the selective integrator in terms of simple linear algebra, discarding most nonlinear and dynamical aspects of the RNN. To begin, we step away from the siRNN for a moment, and instead consider a generic dynamical system

$$\dot{\mathbf{x}} = \mathbf{F}(\mathbf{x}), \tag{4}$$

where the state is defined by the N-dimensional vector, $\mathbf{x}$, and the update rules are defined by $\mathbf{F}$, a vector function. Fixed points are vectors $\mathbf{x}^*$ such that

$$\dot{\mathbf{x}} = \mathbf{F}(\mathbf{x}^*) = \mathbf{0}, \tag{5}$$

so the system is at equilibrium at such a point. Fixed points are either stable or unstable. For a stable fixed point, if the state of the system is started near the fixed point, the state converges to it. For an unstable fixed point, the state diverges away. Stable fixed points are also called attractors, and are the mechanism underlying memories in Hopfield networks[3]. Unstable fixed points are not observed in the siRNN.

Finally, one can also have a line attractor, which is a 1-dimensional manifold (a line, possibly curved) of fixed points with the property that there is zero motion in the direction of the line and decaying dynamics towards the line. A famous example of a line attractor in neuroscience is given by Seung[6], where he explains how the eyes can simultaneously take many positions and are nevertheless kept still. For the siRNN, the purpose of a line attractor is to represent the amount of accumulated evidence towards one choice or another. Since there are two contexts in the siRNN, there are two contextually defined line attractors.

Line attractors require perfect tuning in order to have zero motion along the direction of the line. In practice, such fine tuning does not exist, so a series of fixed points that approximate a line attractor are in fact what we find in the trained siRNN (see Fig. 5 in the main text). On such an approximate line attractor, there are a few true fixed points, i.e. $\dot{\mathbf{x}} = \mathbf{0}$, but mostly there are slow points, i.e. $\dot{\mathbf{x}} \approx \mathbf{0}$, such that there is very mild drift along the line.

Linear approximations

The main reason fixed points are important when trying to understand a nonlinear dynamical system, such as an RNN, is that a region always exists around a fixed point, sometimes

small and sometimes large, where the system can be understood in essentially linear terms, i.e. as a linear dynamical system. We can see this with just a few lines of math involving the Taylor series expansion of the update equations, $\dot{\mathbf{x}} = \mathbf{F}(\mathbf{x})$. Consider the Taylor expansion of $\mathbf{F}(\mathbf{x})$ around a fixed point in state space, $\mathbf{x}^*$:

$$(\mathbf{x}^* \dot{+} \boldsymbol{\delta}\mathbf{x}) = \mathbf{F}(\mathbf{x}^* + \boldsymbol{\delta}\mathbf{x}) = \mathbf{F}(\mathbf{x}^*) + \mathbf{F}'(\mathbf{x}^*)\boldsymbol{\delta}\mathbf{x} + \frac{1}{2}\boldsymbol{\delta}\mathbf{x}\mathbf{F}''(\mathbf{x}^*)\boldsymbol{\delta}\mathbf{x} + \dots \tag{6}$$

Here we have defined the nonlinear system up to second order. Since the system is at a fixed point, the zero order term, $\mathbf{F}(\mathbf{x}^*)$, is equal to $\mathbf{0}$, giving

$$\mathbf{F}(\mathbf{x}^* + \boldsymbol{\delta}\mathbf{x}) = \mathbf{F}'(\mathbf{x}^*)\boldsymbol{\delta}\mathbf{x} + \frac{1}{2}\boldsymbol{\delta}\mathbf{x}\mathbf{F}''(\mathbf{x}^*)\boldsymbol{\delta}\mathbf{x} + \dots \tag{7}$$

If we ensure that $\boldsymbol{\delta}\mathbf{x}$ is small, we can safely ignore second and higher order terms, yielding

$$(\mathbf{x}^* \dot{+} \boldsymbol{\delta}\mathbf{x}) = \mathbf{F}'(\mathbf{x}^*)\boldsymbol{\delta}\mathbf{x} \tag{8}$$

$$\dot{\boldsymbol{\delta}}\mathbf{x} = \mathbf{F}'(\mathbf{x}^*)\boldsymbol{\delta}\mathbf{x} \tag{9}$$

and by simply renaming variables, $\mathbf{y} \equiv \boldsymbol{\delta}\mathbf{x}$ and $\mathbf{M} \equiv \mathbf{F}'(\mathbf{x}^*)$, we end up with the familiar linear form

$$\dot{\mathbf{y}} = \mathbf{M}\mathbf{y}. \tag{10}$$

Thus for small perturbations, $\boldsymbol{\delta}\mathbf{x}$, around a fixed point, $\mathbf{x}^*$, any nonlinear system behaves like a linear system. The fixed points act as a scaffolding for the nonlinear dynamics, allowing us, at least in simple cases, to decompose a hard nonlinear problem into smaller, linear sub-problems. This process is called linearization around a fixed point.

For the siRNN, the matrix $\mathbf{M}(\mathbf{x}^*)$ is obtained by computing $\mathbf{F}'(\mathbf{x}^*)$ for equation (1). Concretely, it is the derivative of $\mathrm{F}_i()$ with respect to x_j, i.e. $\frac{\partial \mathrm{F}_i}{\partial x_j}$, giving

$$M_{ij}(\mathbf{x}^*) = -\delta_{ij} + J_{ij}\ \mathrm{h}'(x_j^*), \tag{11}$$

where δ_{ij} is defined to be 1 if $i = j$ and otherwise 0 [*], and $\mathrm{h}'()$ is the derivative of the nonlinearity $\mathrm{h}()$ with respect to its input. Since this matrix derives from $\mathbf{F}(\mathbf{x})$, it is related to the feedback matrix, $\mathbf{J}$, but it is not $\mathbf{J}$. Instead, $\mathbf{M}$ defines the linear network that approximates the RNN around the point $\mathbf{x}^*$.

Going forward, our notation will drop the explicit dependency of $\mathbf{M}$ on $\mathbf{x}^*$, with the understanding that each locally linear system is still defined in terms of a particular fixed point.

[*]The notation δ_{ij} is the identity matrix written using indices and shouldn't be confused with $\boldsymbol{\delta}\mathbf{x}$.

Combining local linear systems to understand an RNN

As shown in Sussillo and Barak[5], the approach to understanding a trained RNN is to find as many fixed points and approximate fixed points of the system as possible. After finding these points, one linearizes the dynamics around them to understand the local dynamics. One then pieces all the linear solutions together to garner a semi-quantitative view of how the RNN functions. This means that there is always a local approximate linear system in consideration as well as the global, nonlinear system and one should keep these two systems separate conceptually. In what follows, we focus on a single, generic fixed point on a line attractor. Thus the arguments hold for all the fixed points on the line attractor. For the siRNN, this approach is adequate to explain how the system works.

An aside concerning approximate fixed points

Following Sussillo and Barak[5], linearization is appropriate around not only fixed points, but any sufficiently slow point, where a slow point is defined by a small nonzero value of the function $q(\mathbf{x}) = \frac{1}{2}|\mathbf{F}(\mathbf{x})|^2$. The function $q(\mathbf{x})$ defines the squared speed of the system divided by two. The understanding that one can treat slow points (with care) in the same way as true fixed points is important here since the line attractors in the siRNN are approximate, meaning they are lines of mostly slow points with only a few true fixed points. To simplify the explanations in what follows, we will ignore the distinction between a true fixed point and a slow point with the understanding that dynamics around slow points are qualitatively similar to those around true fixed points. Most importantly, the main assumption that linear dynamics are a good local approximation of the nonlinear dynamics still holds around slow points.

Linear systems

Linear dynamical systems can do four things: expand, contract, oscillate, and integrate an input. The last can technically only happen under perfect tuning. Normally, after an input is injected into the system, one thinks of very slow expansion or contraction as approximate integration.

The primary method one uses to understand what a linear system is doing is by diagonalizing the interaction matrix, $\mathbf{M}$, using an eigenvector decomposition. This decomposition is useful because it defines a basis in which certain patterns of activity, i.e. activity in special directions in state space, evolve separately from each other. A right eigenvector, $\mathbf{v}$, satisfies $\mathbf{M}\ \mathbf{v} = \lambda\ \mathbf{v}$, thus the matrix acts on these special vectors in a particularly straightforward way by scaling them by the amount, λ, called the eigenvalue. So the behavior of a linear dynamical system, $\dot{\mathbf{y}} = \mathbf{M}\ \mathbf{y}$, which involves the repeated application of $\mathbf{M}$, becomes easy

to understand as, for example, the expansion (repeated scaling up) or contraction (repeated scaling down) of these vectors. The eigenvectors are a property of the matrix, and for a matrix defined by equation 11, the eigenvector decomposition is

$$\mathbf{M} = \mathbf{R}\,\mathbf{E}\,\mathbf{L} = \sum_{a}^{N} \lambda_a\, \mathbf{r}^a\, \mathbf{l}^a, \tag{12}$$

where λ_a is the a^{th} eigenvalue, $\mathbf{r}^a$ is the a^{th} right eigenvector (a column of $\mathbf{R}$) and $\mathbf{l}^a$ is the a^{th} left eigenvector (a row of $\mathbf{L}$). The matrix $\mathbf{R}$ is the matrix of right eigenvectors collected as columns, $\mathbf{L}$ is the matrix of left eigenvectors collected as rows with the property that $\mathbf{L} = \mathbf{R}^{-1}$. The matrix $\mathbf{E}$ is a diagonal matrix of eigenvalues.[†]

Looking forward, we are interested in the linearized dynamics around a fixed point in the full nonlinear system. To study those linear dynamics, we study $\mathbf{M}$, defined by equation (11), that derives from the original nonlinear system. The way to make sense of $\mathbf{M}$ is to use the eigenvector decomposition, defined by equation (12).

In the basis of the left eigenvectors, the local linear system is diagonalized, meaning the dynamics of the N modes evolve independently of each other. Diagonalizing the local network dynamics around a fixed point proceeds (again with $\mathbf{y} \equiv \mathbf{x} - \mathbf{x}^*$) as follows

$$\dot{\mathbf{y}} = \mathbf{M}\,\mathbf{y} \tag{13}$$

$$\dot{\mathbf{y}} = (\mathbf{R}\,\mathbf{E}\,\mathbf{L})\,\mathbf{y} \tag{14}$$

$$\mathbf{L}\,\dot{\mathbf{y}} = \mathbf{E}\;(\mathbf{L}\,\mathbf{y}) \tag{15}$$

$$\dot{\alpha_a} = \lambda_a \alpha_a, \tag{16}$$

where α_a is the a^{th} component of the vector $\boldsymbol{\alpha} \equiv (\mathbf{L}\,\mathbf{y})$. The independent modes, $\alpha_a(t)$, show how the different patterns, $\mathbf{r}^a$, evolve through time to create the overall population response.

Assuming all the eigenvalues are distinct, the linear dynamical system is trivially solved in this basis, giving

$$\alpha_a(t) = e^{\lambda_a t} \tag{17}$$

$$\alpha_a(t) = e^{\sigma_a t}\ \cos(\omega_a t), \tag{18}$$

where we have split the eigenvalue λ_a into its real and imaginary parts, $\lambda_a = \sigma_a + i\omega_a$, and ignored the constant of integration[‡]. Thus the eigenvalues explain whether or not a particular pattern, $\mathbf{r}^a$, expands - $\sigma_a > 0$, contracts - $\sigma_a < 0$, oscillates - $\omega_a \neq 0$, or integrates - $\sigma_a = 0, \omega_a = 0$.[§]

[†]A right eigenvector satisfies $\mathbf{M}\,\mathbf{r}^i = \lambda_i\,\mathbf{r}^i$ and a left eigenvector satisfies $\mathbf{l}^i\,\mathbf{M} = \lambda_i\,\mathbf{l}^i$.

[‡]The full solution for a complex root is $c_1 e^{\sigma_a t}\ \cos(\omega_a t) + c_2 e^{\sigma_a t}\ \sin(\omega_a t)$, for constant coefficients c_1 and c_2.

[§]Note that the fine-tuning of an integrator that is implemented as a line attractor is expressed in the requirement that both the real and imaginary parts of the integrating dimension must be exactly zero.

So now we know how the system will behave, based on examining the eigenvalues. However, our description of the dynamics is not in the basis of individual neuron activations. The final step is to put everything back in this basis. To get the modes of the system, we applied $\mathbf{L}$ to $\dot{\mathbf{y}}(t)$ to get $\dot{\boldsymbol{\alpha}}(t)$ and then integrated the modes separately. In order to get back the local network state, $\mathbf{y}(t)$, we apply the $\mathbf{R}$ matrix to $\boldsymbol{\alpha}(t)$, since $\mathbf{R} = \mathbf{L}^{-1}$. This gives

$$\mathbf{y}(t) = \mathbf{R}\ \boldsymbol{\alpha}(t). \tag{19}$$

Understanding selective integration

Due to the nature of the local linear systems on the color-context and motion-context line attractors, we can simplify the linearized dynamics far beyond the general eigenvector decomposition given in the last section. The eigenvalue spectra of the local linearized systems all have a common motif: there is a single eigenvalue that is very near to zero, which we call λ_0, and the rest of the eigenvalues have a large negative real part, $\sigma_a \equiv \mathrm{Re}(\lambda_a) \ll 0$, indicating that the respective modes will decay very quickly. A sensible indexing of the modes is to index a from 0 to N-1, since the zero mode turns out to be the only mode of interest.

Imagine the network was instructed to integrate an instantaneous pulse of color input (see cartoon in Fig. 6b in main text), and the system was on the color-context line attractor at a fixed point, $\mathbf{x}^*$. Then the color input pulse to the siRNN pushes the system off the line attractor in the direction of the color input vector. We want to know how much of the pulse of color is integrated, or stated graphically, how far along the color-context line attractor the system travels after a sufficient amount of time for the network to relax back to the line attractor, call it t_∞. Further, we want to understand how a pulse of irrelevant motion input is ignored while the relevant color pulse is integrated. How is it that the pulse of motion input does not move the system along the color-context line attractor?

In this scenario, each mode of the system will be affected by the color pulse according to the degree of projection of the input vector[¶] onto the associated left eigenvector. So the color pulse, $u_c(t)$, which comes into the system through weights, $\mathbf{b}^c$, has the projection onto a given left eigenvector, $\mathbf{l}^a$, of size dot($\mathbf{l}^a$, $\mathbf{b}^c u_c(t)$). We add this input to the differential equation for the independent modes, equation (16), and solve it. Assuming the network

[¶]We present the argument by using the color (or motion) input vector as a simplified proxy for the location of the system after a pulse of color (or motion) input arrives. To be strictly correct, we should instead use the network state after the pulse of input is finished to handle any nonlinear effects of a strong input. For our siRNNs, this mattered little so we continue using the color and motion input vectors.

state is initialized to the local origin, this gives the standard solution[‖]

$$\alpha_a(t) = \text{dot}\,(\mathbf{l}^a,\ \mathbf{b}^c)\, e^{\lambda_a t}. \tag{20}$$

For a single, instantaneous pulse of color input at time 0, all the modes with index $a > 0$ will be transiently perturbed according to the number, dot($\mathbf{l}^a$, $\mathbf{b}^c$), and then quickly decay to zero. So in the long run, we have $\alpha_a(t_\infty) = 0$ for $a > 0$. Since the non-zero modes decay quickly, one can ignore their dynamics altogether. However, $\mathbf{l}^0$, the mode with (approximately) zero eigenvalue does not decay quickly. Instead, $\mathbf{l}^0$ (approximately) integrates the pulse by adding the value dot($\mathbf{l}^0$, $\mathbf{b}^c$) to the previous value of the mode, which was zero since the system started at $\mathbf{x}^*$, the local origin. So for the current time interval, we have

$$\alpha_0(t) = \text{dot}\left(\mathbf{l}^0,\ \mathbf{b}^c\right) e^{0t} \tag{21}$$

$$\alpha_0 = \text{dot}\left(\mathbf{l}^0,\ \mathbf{b}^c\right). \tag{22}$$

Thus, the local linear dynamics around each fixed point can be approximated as 1-dimensional and static, having only a single mode that integrates the projection of the relevant input onto the selection vector, $\mathbf{l}^0$. We call $\mathbf{l}^0$ the *selection vector* because it is the projection of the input, either color or motion, onto this vector that determines whether or not that input will be integrated or dynamically deleted. We reemphasize that there is no decay along this vector. Thus if an input projects onto it, it will remain in the system. Clearly, the orientation of such a vector is a very powerful determinant in deciding what inputs are, or are not, relevant. If the projection of an input is large, then the amount of integration of that input will be large, if the projection is zero, the amount of integration of that input will be zero.

To understand the final state of the local system in response to a pulse of color input, we project back into the original local space by multiplying with $\mathbf{r}^0$, the local *line attractor*, giving

$$\mathbf{y}(t_\infty) = \mathbf{r}^0\, \text{dot}\left(\mathbf{l}^0,\ \mathbf{b}^c\right). \tag{23}$$

In words, equation (22) states that the *amount* of integration is given by the projection of the input onto the selection vector, yielding a number. Equation (23) states that this amount is *represented* by the local system by advancing along the line attractor by exactly that amount.

Equation (23) determines the amount of integration of a pulse of color input and its representation in state space, while entirely ignoring the linear (or nonlinear) dynamics. Of course, the transient dynamic of the system from its deflection caused by the color pulse, back to the color-context line attractor, $\mathbf{r}^0$, results from the decay of activity on $\mathbf{r}^a$, for $\alpha > 0$.

[‖]The full solution is $\alpha_a(t) = \alpha_a(0)\, e^{\lambda_a t} + \int_0^t e^{\lambda_a (t-t')}\ (\mathbf{l}^a\ \mathbf{b}^c)\ u_c(t')\, dt'$. We set the initial condition, $\alpha_a(0)$, to 0 since we are interested in a pulse from the current fixed point, $\mathbf{x}^*$, which is the origin of the current local linear system. The input pulse is treated as a Dirac delta function at time 0, yielding equation 20.

Note that the long-time solution for a generic color input is

$$\mathbf{y}(t_\infty) = \mathbf{r}^0 \int_0^{t_\infty} \mathrm{dot}\left(\mathbf{l}^0, \mathbf{b}^c\right)\, u_c(t)\, dt, \tag{24}$$

which makes clear that the selection vector determines the integrand and the line attractor determines the direction of the integral in state space.

Finally, to get back the absolute position in state space, we "leave" the local linear system by adding back the local origin, $\mathbf{x}^*$. The new absolute position on the global color-context line attractor is $\mathbf{x}(t_\infty) = \mathbf{x}^* + \mathbf{y}(t_\infty)$ **. This results in a new position on the global color-context line attractor. The change in the local state given by equation (23) represents a good approximation of the total change in state of the full nonlinear siRNN resulting from the integration of a single pulse of color information.

Note that if the matrix of linearized dynamics around the fixed point were normal (e.g. a symmetric matrix, with $\mathbf{M} = \mathbf{M}^\mathrm{T}$, is normal), then both $\mathbf{R}$ and $\mathbf{L}$ would be composed of orthonormal vectors and $\mathbf{L} = \mathbf{R}^\mathrm{T}$. Equation 24 would instead be

$$\mathbf{y}(t_\infty) = \mathbf{r}^0 \int_0^{t_\infty} \mathrm{dot}\left(\mathbf{r}^0, \mathbf{b}^c\right)\, u_c(t)\, dt. \tag{25}$$

Equation 25 corresponds to the familiar notion that in order to integrate an input, (i) the input should project onto the line attractor, $\mathbf{r}^0$; (ii) that the amount of integration corresponds to the size of the projection onto the line, $\mathrm{dot}(\mathbf{r}^0, \mathbf{b}^c)$; and (iii) that the representation in state space of this integrated input is a deflection along the line, $\mathbf{r}^0\,\mathrm{dot}(\mathbf{r}^0, \mathbf{b}^c)$. While intuitive, this is not true for the linear systems in the siRNN, because equation (11) does not in general generate normal matrices.

In the general case, which is applicable to the siRNN, the only requirements on the pair $(\mathbf{r}^0, \mathbf{l}^0)$ is that they are not orthogonal and their dot product equals 1. This leads to an additional degree of freedom that the network has regarding which direction in state space it chooses to integrate. The network architecture may be configured such that $\mathbf{l}^0$ can point in any direction, so long as its not orthogonal to $\mathbf{r}^0$††. Any input in the direction of $\mathbf{l}^0$ will be integrated on $\mathbf{r}^0$. Selective integration as implemented here is as simple as making sure that $\mathbf{l}^0$ is pointed towards the input to be integrated and orthogonal to the input to be ignored. The counterintuitive part is that the neural activations reflect this integration using a different vector, $\mathbf{r}^0$. See Fig. 6b in the main text for an illustration of the interaction of the left and right eigenvectors to achieve selective integration.

Putting it all together, for the global line attractor defined by the color context, the $\mathbf{l}^0$ vectors of the local linear systems are pointed towards the color input vector and are roughly

**This statement is true only if the linear approximation is a perfect description of the global dynamics. Otherwise, there will be some small error.

††While arranging that $\mathbf{l}^0$ be nearly orthogonal to $\mathbf{r}^0$ (e.g. 89.9°) is possible, it is a very poor choice. The requirement that $\mathrm{dot}(\mathbf{l}^0, \mathbf{r}^0) = 1$ would dictate that the norm of $\mathbf{l}^0$ be gigantic, leading to many problems, such as integrating noise in other dimensions.

orthogonal to the motion input vector. This simultaneously explains both the integration of color and the dynamic deletion of the irrelevant motion input. The correct amount of color input is projected onto a mode with no decay, and motion input is projected exclusively into directions of fast decay. In the motion context, the global motion-context line attractor is active. In this case the $\mathbf{l}^0$ vectors associated with the motion line attractor are pointed towards the motion input vector and are approximately orthogonal to the color input vector. In either context, due to the flexibility of the local color and motion $\mathbf{l}^0$ vectors, the two global line attractors need not be precisely aligned to their respective relevant input vectors (see Fig. 6c in main text).

Finally, we address whether treating the nonlinear RNN as a set of linear systems around fixed points is sufficient for explaining its integration and gating mechanisms. We examine this question quantitatively by computing the relative sizes of the zero-order, $|\mathbf{F}(\mathbf{x}^*)|$, first-order, $|\mathbf{F}'(\mathbf{x}^*)\boldsymbol{\delta}\mathbf{x}|$, and second-order, $|\frac{1}{2}\boldsymbol{\delta}\mathbf{x}\mathbf{F}''(\mathbf{x}^*)\boldsymbol{\delta}\mathbf{x}|$, parts of the Taylor series expansion around all the fixed points on the color-context line attractor. For the the color pulse (magnitude of 2.0) in the color context, averaged across all fixed points, the values of the Taylor series terms are (mean ± std) 0.006 ± 0.004, 0.575 ± 0.002, 0.009 ± 0.001, respectively. For a motion pulse in the color context, the values are 0.006 ± 0.004, 0.660 ± 0.004, 0.013 ± 0.001, respectively. So for both motion and color pulses, which result in a deflection in state space of the same order of magnitude as the noisy input during normal operation, the linear part of the Taylor expansion is far larger than either the zero-order or second-order terms. This demonstrates that our linear systems approach is sufficient to explain the operation of the RNN. Analogous results hold for the motion context.

In summary, analysis of the siRNN suggests that a simplified (but still useful) view of how RNNs work is that of a state space tiled with linear systems. These linear systems are responsible for locally linear dynamic computations and have large volumes where the linearity assumption is valid. The nonlinearity of the system is then activated by inputs or internal dynamics that drive the system from one linear system to another.

References for the mathematical explanation

1. Wilson, H. & Cowan, J. Excitatory and Inhibitory Interactions in Localized Populations of Model Neurons. *Biophysical Journal* **12**, 124 (1972).
2. Wang, X. J. Decision making in recurrent neuronal circuits. *Neuron* **60**, 215234 (2008).
3. Hopfield, J. J. Neural networks and physical systems with emergent collective computational abilities. *Proc Natl Acad Sci USA* **79**, 25542558 (1982).
4. Martens, J. & Sutskever, I. Learning recurrent neural networks with hessian-free optimization. Proceedings of the 28th International Conference on Machine Learning *(ICML)* (2011).
5. Sussillo, D. & Barak, O. Opening the black box: low-dimensional dynamics in high-dimensional recurrent neural networks. *Neural Computation* **25**, 626649 (2013).
6. Seung, H. S. How the brain keeps the eyes still. *Proc Natl Acad Sci USA* **93**, 1333913344 (1996).